Cement and Concrete Research 178 (2024) 107463

Contents lists available at ScienceDirect

Cement and Concrete Research

journal homepage: www.elsevier.com/locate/cemconres

In situ synchrotron powder diffraction study of LC^3 cement activation at very early ages by C-S-H nucleation seeding

Alejandro Morales-Cantero [a], Angeles G. De la Torre [a], Ana Cuesta [a], Isabel Santacruz [a], Isabel M.R. Bernal [a], Oliver Mazanec [b], Alessandro Dalla-Libera [c], Pere Borralleras [d], Miguel A. G. Aranda [a,*]

[a] Departamento de Química Inorgánica, Cristalografía y Mineralogía, Universidad de Málaga, Málaga 29071, Spain
[b] Master Builders Solutions Deutschland GmbH, Albert-Frank Str. 32, 83308 Trostberg, Germany
[c] Master Builders Solutions Italia Spa, Via Vicinale delle Corti, 21, 31100 Treviso, Italy
[d] Master Builders Solutions España S.L.U., Carretera de l'Hospitalet, 147-149, Edificio Viena, 1ª planta, 08940 Cornellà de Llobregat, Spain

ARTICLE INFO

Keywords:
CO_2 footprint
Accelerators
Admixtures
C-S-H gel
Ettringite
Rietveld analysis

ABSTRACT

Limestone Calcined Clay Cements, LC^3, are being widely researched as low-carbon binders. However, the hydration reactions during the first day are key for their performances and they were not well known. Here, we employ *in situ* synchrotron X-ray powder diffraction to understand the hydration reactions that take place during the first day. The influence of two superplasticisers and three strength-enhancing admixtures have been investigated. The diffraction data were analysed by the Rietveld method and the results compared to mass balance calculations. For LC^3 binders and in the absence of strength-enhancing admixtures, the hydration rates of the clinker phases, *i.e.* C_3S, C_3A and C_4AF, are accelerated because of the filler effect. The C-S-H based-admixtures further accelerate the hydration of tricalcium aluminate and ferrite. Chiefly, it is firmly proved that the pozzolanic reaction takes place from 7 h onwards in the studied experimental conditions. The estimated degree of hydration of metakaolin at 22 h, in the studied binders, was ~10 %.

1. Introduction

Portland cement (PC) world production was in 2019–4 Gt/yr [1], being the main constituent of concretes [2]. On average, every ton of Portland clinker generates ~0.87 tons of CO_2 [3] which accounts for ~8 % of all anthropogenic CO_2 emissions [4]. CO_2 footprint decrease in the cement industry has been recognized as critical [4–7] but it is also acknowledged that it is very difficult to attain [8]. A principal work [6] concluded that clinker replacement by supplementary cementitious materials (SCMs) [9,10] is the most advantageous current way for CO_2 footprint decrease, having the lowest performance and economic impacts.

Widely-available kaolinitic calcined clays are gaining increased attention as SCMs [10]. However, the main drawback of the resulting limestone calcined clay cements (LC^3) [11–13] is their poor mechanical strengths at early ages, *i.e.* 1–3 days. Therefore, it is important to enhance/accelerate cement hydration at early ages. This is a common requirement shared by several other low-carbon cements [14,15] where SCMs are used to increase the clinker replacement factor [4,9,10,12]. Although there are several ways to improve the early hydration of cements, not all of them are compatible with keeping the mechanical strength and durability performances, and at the same time using highly available, sustainable and cost-effective products. Here, we focus on nucleation seeding by water-based stabilised suspensions of C-S-H nanoparticles [16–18]. It must be noted that a synergistic effect between C-S-H seeding and alkanolamine addition is being reported [19–25] for enhancing the hydration of low-carbon cements. Hereafter, cement nomenclature will be employed to describe the different phases. On the one hand, C-S-H nucleation seeding slightly accelerates C_3S hydration and mainly enhances C-S-H nucleation in the pore solution (outer product C-S-H) at the expense of C-S-H covering alite particles (inner product C-S-H), which results in a more homogenous distribution of C-S-H gel with lower capillary porosities [26]. On the other hand, it is known that alkanolamines accelerate the C_3A and C_4AF hydration and that its dosage is quite important as higher amounts can hinder PC hydration.

There are several reviews on the use of stabilised C-S-H nanoparticles

* Corresponding author.
E-mail address: g_aranda@uma.es (M.A.G. Aranda).

https://doi.org/10.1016/j.cemconres.2024.107463
Received 17 April 2023; Received in revised form 10 January 2024; Accepted 13 February 2024
Available online 22 February 2024

in cement hydration [26–28] and it is beyond the scope of this article to review this topic further. The most recent review [26] focused on the use of commercial C-S-H nucleation seeding admixtures in low-carbon cements, mainly blends of PC with SCMs. It was shown that the improvements in the mechanical strength performances observed at 12 h, 1 and 28 days of hydration vary but are close to +100 %, +50 % and + 20 % respectively. In any case, the optimum C-S-H admixture dosage is binder and application dependent. To better understand the mechanism of C-S-H seeding, X-ray powder diffraction (XRPD) data analysed by the Rietveld method is key to showing the hydration degree of the different phases. It is noted that calorimetry is being widely used but it only gives an overall picture as the signal is the compounded function of all hydration reactions. To the best of our knowledge, so far only two works report *in situ* Rietveld quantitative phase analyses (RQPA) for C-S-H seeded samples at early hydration ages [19,29]. From laboratory XRPD data, it was reported faster dissolution rates of C_3S, C_3A and anhydrite for the seeded PC blends with ground granulated blast furnace slag [29]. The second work [19] employed *in situ* synchrotron XRPD (SXRPD) to study the early age hydration reactions for C-S-H seeded PC 42.5 R pastes, water-to-cement mass ratio (w/c) of 0.50. The data were taken in transmission within rotating capillaries. This approach is free from the three most common experimental errors in LXRPD working in reflection with pastes covered by a foil (◆ water microbleeding, ◆ Portlandite preferred orientation, ◆ vertical particle segregations before setting). This work showed that the alite hydration was slightly accelerated by C-S-H nucleation seeding. Moreover, C-S-H seeding also enhanced C_3A and C_4AF dissolutions, principally after 10 h. As expected, enhanced gypsum and C_3A dissolutions resulted in larger amounts of crystallised ettringite. It should be noted that C-S-H nucleation seeding is already being employed for cement hydration acceleration and microstructural optimization of LC^3 type cements [22,30–35]. C-S-H seeding seems to be specially adequate for boosting the mechanical strength performances of LC^3 binders at one day of hydration [33,35,36].

Here, we expand our initial work [19] to study the C-S-H seeding of PC 52.5 R pastes (w/c = 0.50) and then to LC^3 binders, based on this PC, with w/b = 0.40 (w/b refers to water-binder mass ratio). The hydration of these binders has been enhanced with two C-S-H commercial admixtures and with triisopropanolamine (TIPA), a commonly used cement additive. To extract the best possible information from the RQPA results, mass balance calculations have also been carried out. This is even more important for LC^3 C-S-H seeded pastes where the pozzolanic reactions have been investigated. Therefore, the next section summarises the basic knowledge about the most common hydration reactions.

2. Hydration reactions for mass balance calculations

Establishing the cement hydration reactions allows us to carry out mass balance calculations, under some assumptions, that is important to understand the sequences of chemical processes taking place with time. Firstly, we focus on the chemical reactions for the clinker phases, see Annex: Table A1. The reactions are described for gypsum but adapting them for bassanite or anhydrite is straightforward. Eq. (1) gives alite hydration [2,37,38]. It must be noted that the average C/S ratio within C-S-H gel as well as its water content at the micrometre scale is variable. In (1), a C/S ratio of 1.8 and a H/S ratio of 4.0 are assumed [38]. Belite hydration does not take place at early ages and therefore is not discussed here. Eq. (2) details C_3A hydration in the presence of sulfates [2,37] to yield ettringite. The hydration of C_4AF is slower and more complicated as the main iron-containing hydrated phase(s) are amorphous. Amorphous siliceous hydrogarnet (named here as Fe-Si-H) has been reported as the most stable phase from C_4AF hydration in PCs [39,40]. Therefore, eq. (3a) has been previously used for mass balance calculations [41,42]. This hydration reaction, at early ages, was supported by a recent *in situ* SXRPD, where alkanolamine boosted C_4AF dissolution which was accompanied by larger amounts of ettringite [19]. However, at later hydration ages, one week or later, the reaction of C_4AF does not produce ettringite. This is very likely due to the lack of available sulfates. Therefore, the related eq. (3b), yielding aluminium-siliceous hydrogarnet was proposed [43] and it is given here for completeness, but not used.

Secondly, we deal with the pozzolanic reactions, see Annex: Table A2. In calcined kaolinitic clays, the main pozzolanic compound is metakaolin (MK). Here, we describe metakaolin by its ideal composition, $Al_2Si_2O_7$, although we are aware that it has a complicated local structure, without long-range order, and it may contain some residuals hydroxide groups [44–46]. The hydration reaction pathway(s) of SCMs in general, and MK in particular, depends upon the overall composition of the hydrating blend [47,48]. The reactions in absence of sulfates/carbonates, give stratlingite and/or hydroxide-AFm type phases. These reactions are not relevant here. At early hydration ages, AFm-type monocarboaluminate (Mc or $Ca_4Al_2(OH)_{12}(CO_3)(H_2O)_5$) is normally not detected, and ettringite and/or hemicarbonate (Hc or $Ca_4Al_2(OH)_{13}(CO_3)_{0.5}(H_2O)_{5.5}$) are formed. Thus, eqs. (4a), (4b) and (4c) detail the hydration of MK to give AFt, Hc, or both; in the presence of sulfate-rich and sulfate-poor pore solutions. Specifically, eq. (4a) describes the hydration of MK with sulfates to give C-A-S-H and ettringite. Eq. (4b) details the hydration of MK with carbonates to give C-A-S-H and Hc. Eq. (4c) is an intermediate situation where the hydration of MK may yield C-A-S-H, AFt and Hc, which is not used here but given for completeness. Eq. (5) is the related one to yield Mc in absence of sulfates, which is not used here as Mc is not observed at early ages.

3. Materials and methods

3.1. Starting material provenance

The PC used in this study was a CEM I 52.5 R, PC-52.5, from Financiera y Minera S.A. (Málaga, Spain) which conforms to EN 197–1. 20 kgs of the commercial kaolinite-rich clay supplied by Arcimu, S.A. (Zaragoza, Spain), reference CVPM3B (2021), were crushed (2 mm mesh) and calcined at 860 °C for 4 h at Inducerama brick-manufacturing company (Malaga). This temperature is the operational one that could not be changed. After calcination, the calcined clay (CC) was milled up to a $D_{v,50}$–13 μm. A commercial limestone (LS), reference Omyacarb® 5F, was provided by Omya Clariana S.L.U. (Granada, Spain). A commercial gypsum (Gy) supplied by Fábrica de yesos y escayolas La Maruxiña S.A. (Toledo, Spain) was used. The Supplementary Information (S.I.) gives the analyses of the employed materials.

This study was performed with plain PC-52.5 and with LC^3 binder. The LC^3 blend contained 52 wt% of PC-52.5, 30 wt% of the CC, 15 wt% of LS, and 3 wt% Gy as detailed in Table 1, see below.

The cement was analysed by XRF, SXRPD, thermal analysis, laser diffraction, nitrogen isotherm and Blaine air permeability. Its full characterisation is deposited in S.I. The elemental and mineralogical compositions are given in Tables S1 and S2, respectively. Fig. S1 reports the thermal analysis traces for determining the gypsum and bassanite contents. The textural properties are also reported, see Table S3 and Fig. S2. The Blaine and density values were 451(3) m^2kg^{-1} and 3.096(1) $g{\cdot}cm^{-3}$, respectively.

The kaolinite content of the 105 °C-dried raw clay was determined from three approaches. Firstly, from the weight loss in the thermal analysis study, see Fig. S3. The measured mass gave a kaolinite content of 76.3 wt%. Secondly, from the Rietveld analysis of the powder pattern by using the internal standard methodology, see Fig. S4. The full mineralogical composition is given in Table S4, which includes a crystalline kaolinite content of 72.9 wt%. Finally, the kaolinite content was also estimated from the XRF analysis. In this case, from the total Al_2O_3 content (Table S1), it was subtracted the amount of aluminium oxide within the crystalline phases quantified in the Rietveld study, excluding kaolinite. Then, the resulting Al_2O_3 amount was assumed to fully come from kaolinite, which was 74.2 wt%. The reported final kaolinite content, 74 wt%, is the average of these three measurements. We do not

Table 1
Summary of all the pastes prepared in this work with the dosages and the acronyms. The admixture dosages are referred to the anhydrous binder.

	PC /g	CC /g	LS /g	Gy /g	H_2O /g	SP /g	XS130 /g	STE53 /g	TIPA /g	w/c w/b
PC-52.5-w/c=0.50-Ref	100	–	–	–	50.00	–	–	–	–	0.50
PC-52.5-w/c=0.50-STE53	100	–	–	–	48.56	–	–	2.00	–	0.50
PC-52.5-w/c=0.40-SP1-Ref	100	–	–	–	39.72	0.43[$]	–	–	–	0.40
PC-52.5-w/c=0.40-SP1-XS130	100	–	–	–	38.28	0.43[$]	2.00	–	–	0.40
PC-52.5-w/c=0.40-SP1-STE53	100	–	–	–	38.28	0.43[$]	–	2.00	–	0.40
PC-52.5-w/c=0.40-SP1-TIPA	100	–	–	–	39.72	0.43[$]	–	–	0.05	0.40
LC^3-w/b=0.40-SP1-Ref	52	30	15	3	39.72	0.43[$]	–	–	–	0.40
LC^3-w/b=0.40-SP1-XS130	52	30	15	3	38.28	0.43[$]	2.00	–	–	0.40
LC^3-w/b=0.40-SP1-STE53	52	30	15	3	38.28	0.43[$]	–	2.00	–	0.40
LC^3-w/b=0.40-SP1-TIPA	52	30	15	3	39.72	0.43[$]	–	–	0.05	0.40
LC^3-w/b=0.40-SP2-Ref	52	30	15	3	39.72	0.43[#]	–	–	–	0.40
LC^3-w/b=0.40-SP2-XS130	52	30	15	3	38.28	0.43[#]	2.00	–	–	0.40
LC^3-w/b=0.40-SP2-STE53	52	30	15	3	38.28	0.43[#]	–	2.00	–	0.40
LC^3-w/b=0.40-SP2-TIPA	52	30	15	3	39.72	0.43[#]	–	–	0.05	0.40
LC^3-Gy2-w/b=0.40-SP1-Ref	52	30	15	3[*]	39.72	0.43[$]	–	–	–	0.40

[$] Amount of SP1.
[#] Amount of SP2.
[*] This gypsum was Gy2 which has $D_{v,50}$~13 μm.

report decimal places as the variability of natural materials is larger than 1 %. This raw clay was calcined as detailed in methods and milled. The textural properties of the resulting solid, CC, are given in Table S3.

The mineralogical compositions of the employed LS and Gy samples were given in Table S4 and the textural properties in Table S3. It is noted that there are two gypsum samples. Gy-1 was prepared by grinding in a ball mill the as-received sample for 1.5 h stopping every 30 min, waiting for 30 min to avoid overheating. The *in situ* SXRPD showed that this gypsum sample, Gy-1, did not fully dissolve during the first day, see below. This gypsum sample, Gy-1, had a $D_{v,50}$~33 μm. Thus, a new batch, Gy-2, was prepared grinding for 4.0 h, stopping every hour and waiting for 30 min to avoid overheating. This sample, Gy-2, had a $D_{v,50}$~13 μm. The powder pattern for Gy-2 is reported in Fig. S5, where there are no diffraction peaks from bassanite. The textural properties of Gy-1 and Gy-2 are also reported in Table S3 and the PSD traces are given in Fig. S2.

Quartz (SiO_2 of 99.5 %, AlfaAesar) was used as the internal standard in the powder diffraction experiments to indirectly quantify the overall amount of amorphous and unidentified components (ACn). To do so, 12.0 wt% of quartz was manually added, in an agate mortar, to the required dried mixtures before the experiments [49]. For the calculations, the standard was assumed to be 100 % crystalline quartz.

Two polycarboxylate-ether based superplasticisers (SP) have been employed: SP-1 which is a standard one commonly used for concrete rheology optimisation and SP-2 which is a new superplasticiser specially designed to avoid the loss of fluidity during the first hours of LC^3 hydration. These SPs have been already employed for processing unseeded and C-S-H seeded LC^3-mortars [35,36].

The employed accelerating admixtures, also known as strength-enhancing admixtures, were: i) triisopropanolamine (98 %, Acros Organics), ii) Master X-Seed 130 (XS130) and iii) Master X-Seed STE53 (STE53). XS130 and STE53 are C-S-H gel-based seeds with solid contents close to 28 wt%, from Master Builders Solutions España S.L.U., Spain. A description of these C-S-H nucleation seeding admixtures have been recently reported [20].

3.2. Paste preparation

All the pastes were prepared in the same way for the *in situ* X-ray powder diffraction (XRPD) studies and the isothermal calorimetry studies. Table 1 gives the dosages of all pastes including their water and admixture contents.

A first set of pastes was prepared with water/cement mass (w/c) ratio of 0.50 following the methodology reported elsewhere [19]. The *in situ* synchrotron XRPD, at 25(1) °C, and the calorimetry studies were performed for the neat PC-52.5 and the accelerated paste by adding STE53.

A second set of pastes, for LC^3 binders, was prepared with w/b of 0.40. Firstly, the 80 % of the total water was added to the binder and stirred for 1 min at 800 rpm. Secondly, the employed amount of SP was added with a syringe and 10 % of the total water, to flush out any SP left in the syringe, was also added and the paste was stirred for 1 min at 800 rpm. Thirdly, the accelerator admixture was added and immediately the remaining 10 % of the total water was used to flush out any accelerator left in the syringe. The paste was again stirred for 1 min at 800 rpm. The reference pastes, without accelerator, were prepared following the same methodology except that in the second step the SP was added with the 20 % of the total water and with 2 min of mechanical stirring at 800 rpm. Finally, all the pastes were injected, with the aid of a syringe, in glass capillaries of 0.70 mm of diameter for *in situ* Synchrotron and Laboratory XRPD studies or placed into the glass ampoules for the calorimetries.

After some preliminary tests, the amount of SP added for all the pastes was 0.43 wt% (as received) by weight of binder *(bwb)*. This amount was chosen to have pastes with good fluidity, to fill the narrow capillaries, but without any feature of segregation. The accelerators were added at 0.05 wt% *bwb* of TIPA and 2.0 wt% *bwb* (as received) for XS130 and STE53. The water contents of all the admixtures were taken into account to maintain fixed the w/b ratios, *i.e.* 0.40 for LC^3 pastes and 0.50 for PC pastes.

3.3. Analytical techniques

3.3.1. X-ray fluorescence analysis

Data were taken in an ARL ADVANT'XP+ Thermo Fisher device, in fused beads.

3.3.2. Textural characterisation

Three textural features were measured: i) Specific surface area from BET calculations of N_2 isotherms (ASAP 2420, Micromeritics, USA); ii) air permeabilities following EN 196–6 (Blaine fineness device from Controls); iii) Particle size distribution (PSD) by laser diffraction. The PSD data were measured in a Mastersizer 3000 equipment (Malvern Panalytical) using a dry chamber (Aero S). The MIE-non-spherical methodology was adopted to treat the raw data. The refractive and absorption indexes are given in Table S5 in S.I.

3.3.3. Transmission Electron Microscopy (TEM) study

A JEM-1400 (Jeol, Japan) microscope working at 80 kV with a camera Gatan ES1000W, was used to characterize the particle size and morphology of STE53 admixture. A diluted suspension (1/1000) with isopropanol was prepared and further dispersed within an ultrasound bath for 10 s. The resulting diluted suspension was dropped on Cu grids (200 mesh) with formvar-carbon films.

All the above equipments are located at SCAI–Universidad de Málaga.

3.3.4. Isothermal calorimetry

A Thermal Activity Monitor (TAM) instrument (8 channel) was used. Subsection 3.2 described the paste preparation methodology. The measurements took 7 days at 20 °C, excluding the first 45 min after mixing, which is required for thermal stabilisation.

3.3.5. In situ Synchrotron X-Ray Powder Diffraction (SXRPD)

The MSPD beamline (ALBA synchrotron, Spain) [50] was used for the *in situ* SXRPD study. The diffractometer is equipped with MYTHEN detector yielding very good signal-to noise ratios for short measurement times. The used wavelength was 0.61907(1) Å (20 keV) and the temperature in the experimental hutch was 25(1) °C. The temperature of the pastes within the capillaries was not measured. However, the capillaries were narrow, 0.7 mm of diameter, and therefore thermal dissipation is high. As a result, the temperature of the pastes should be quite close to 25 °C. The capillaries were spun at 20 rpm during data collection and the four capillaries sample holder was used. Each pattern took 6 min [angular range from 2 to 40° (2θ)] and three positions along each capillary were measured and then merged to have better statistics and powder averaging. The hydration period from ~0.5 h (required to prepare the paste, fill the capillaries up and close the experimental hutch) to ~24 h was continuously monitored for all the pastes. For selected pastes, some patterns were collected at longer times if synchrotron beamtime was available, *i.e.* for the pastes scanned at the beginning of the synchrotron experiment.

GSAS-II software [51] was used to carry out the Rietveld quantitative phase analyses (RQPA) for the SXRPD patterns as published elsewhere [19]. The ACn values determined by the internal standard methodology [49], include the free water (FW), the increasing C-S-H or C-(A)-S-H gels contents (from the hydration of alite and the pozzolanic reaction), and any other amorphous components (for instance any ill-crystallised hydrated phase like AFm or siliceous hydrogarnet).

3.3.6. In situ laboratory x-ray powder diffraction (LXRPD)

To check the effect of the particle size of the employed gypsum, a LC^3 paste with fine gypsum with $D_{v,50}$~13 μm was prepared in the same way as detailed in subsection 3.2, including quartz as internal standard. An *in situ* LXRPD study was performed in a D8 ADVANCE (Bruker AXS) powder diffractometer located at SCAI–Universidad de Málaga with Mo-Kα_1 radiation, $\lambda = 0.7093$ Å, working with the capillary configuration [52] at 28(1) °C. The paste was introduced in a 0.7 mm diameter capillary that was rotated during data collection. The powder patterns were continuously collected from ~0.5 to ~35 h. Each pattern took 2.3 h in the angular range of 3 to 35°(2θ). These patterns were analysed by Rietveld method using the GSAS and the EXPGUI graphic interface [53].

4. Results and discussion

4.1. Characterisation of the C-S-H admixtures

A detailed characterisation of the C-S-H nucleation admixture can be found in the original patent [54]. TEM was used to characterize the morphologies and the particle sizes of STE53 seeds. Fig. 1 shows a large view of the dispersed C-S-H seed displaying partly agglomerated particles with variable sizes ranging 50–500 nm. The enlarged view shows many small C-S-H domains within one agglomerated particle. Analogous particle sizes have recently been reported for XS130 [19,55] and the related admixture, Master X-Seed 100 [19,56].

4.2. In situ calorimetric study of pastes

Fig. 2 shows the calorimetric data highlighting the effects of the used admixtures: superplasticisers and cement hydration accelerators. Fig. 2a and d show the calorimetric curves for the PC-52.5 pastes processed with SP1. The hydration took place under two conditions: i) w/c = 0.50 without SP, to be related to our previous work which used SXRPD and calorimetry for studying cement hydration activation at early ages by C-S-H seeding [19]; and ii) w/c = 0.40 and SP1, because this w/b ratio is

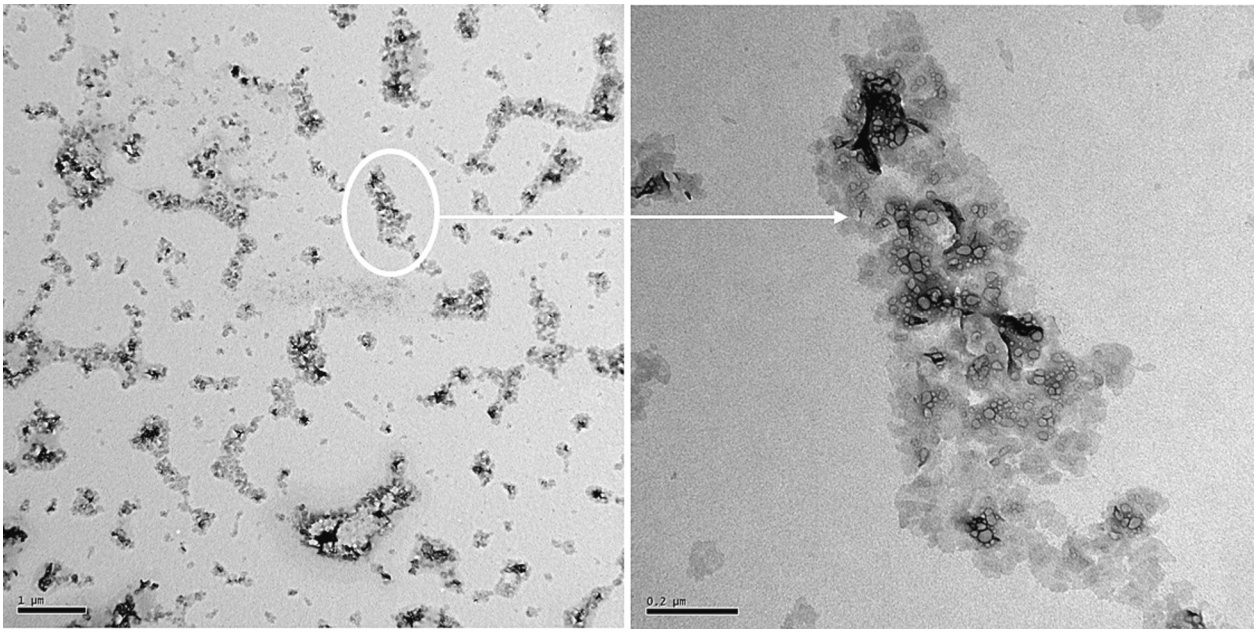

Fig. 1. TEM images for the employed STE53 admixture. (Left) Selected large field-of-view for the C–S–H nucleation seeds dispersed in isopropanol. (Right) Magnified view showing an agglomerated cluster with individual particles smaller than 100 nm.

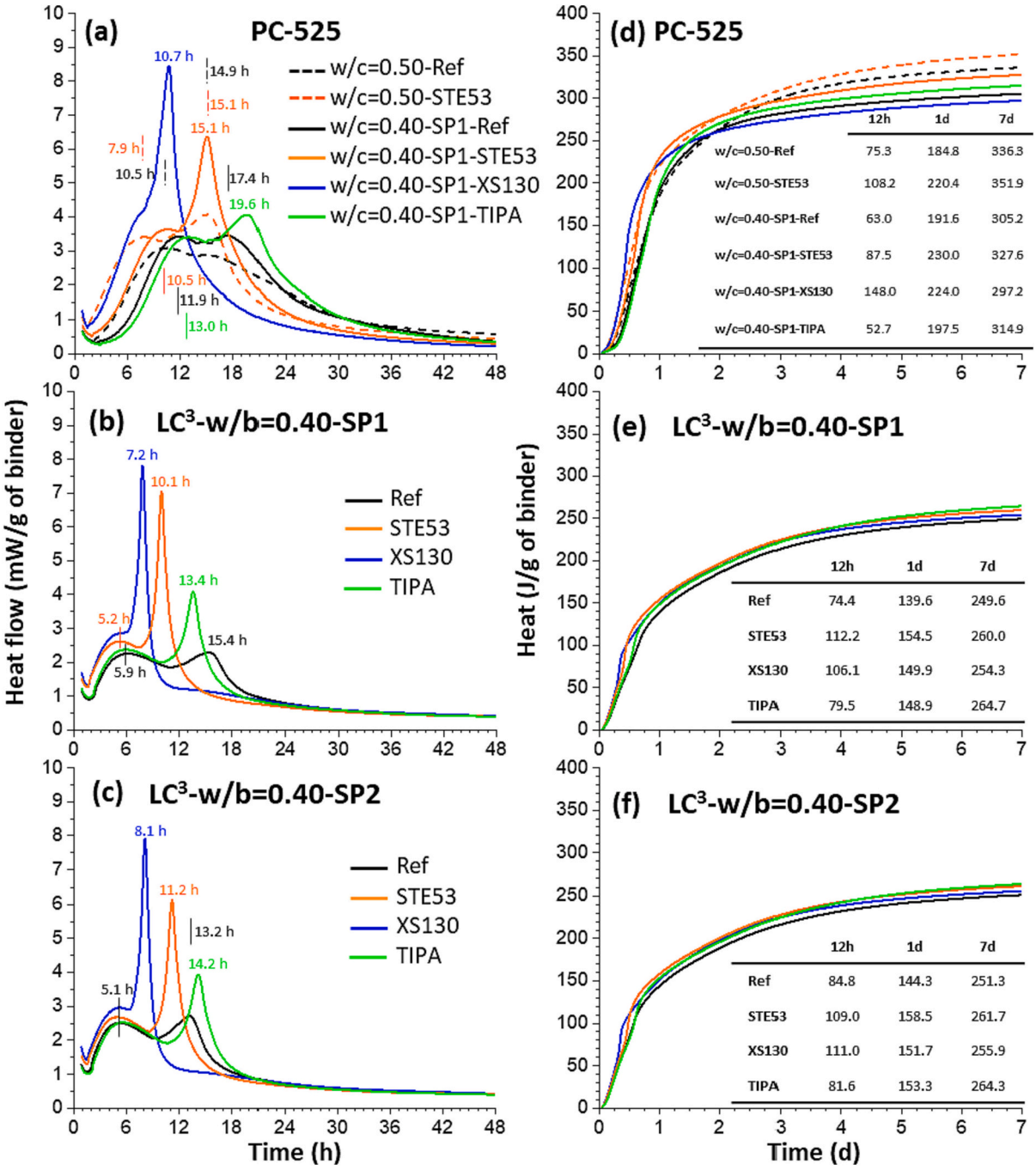

Fig. 2. Calorimetries ($T = 20$ °C) for the studied pastes, referenced to the mass of dried binder, showing the effects of the accelerator admixtures. *Left panels:* The first two-day heat flow traces for better visualization. *Right panels:* Cumulative heat developed during the first week of hydration. The total heats (J/g) at 12 h, 1d and 7 d of hydration are given in the insets for comparison. (a) Heat flows for PC-52.5 pastes with w/c = 0.40 and SP1, and with w/c = 0.50 without *SP*. The corresponding cumulative heats are displayed on (d). (b) Heat flows for LC^3 binders with w/b = 0.40 and SP1, and their cumulative heats on (e) panel. (c) Heat flows for LC^3 binders with w/b = 0.40 and SP2, and their cumulative heats on (f) panel. (For interpretation of the references to colour in this figure legend, the reader is referred to the web version of this article.)

commonly employed for LC^3 studies. On the one hand, at $T = 20$ °C and w/c = 0.50, the effect of STE53 was shortening the induction period and boosting the aluminate peak. On the other hand, the changes by C-S-H seeding at w/c = 0.40 are more conspicuous. The reference paste has the alite and aluminate peaks centred at 11.9 and 17.4 h, respectively. TIPA slightly enlarged the induction period and increased the aluminate peak area. Conversely, both STE53 and XS130 admixtures strongly decrease the induction period, as expected [26,27,57]. It is noted that the paste containing XS130 is almost undersulfated. This highlights that, in order to have properly sulfated binders, the admixture nature and content should also be taken into account. Moreover, the most important effect of C-S-H seeding is the acceleration and enhancement of the aluminate peaks, see Fig. 2a.

Fig. 2b and e show the calorimetric curves for the LC^3 pastes processed with SP1. The reference paste was hydrated without any accelerating admixture and the main peaks for alite and the aluminates took place at 5.9 and 15.4 h, respectively. It should be noted that the aluminate peak is not very much accelerated with respect to PC-52.5,

which takes place at 17.4 h. Conversely, the alite peak is very much accelerated, *i.e.* PC-52.5 displayed this peak at 11.9 h. This acceleration is most likely due to the filler effect caused by the small particle size of the used SCM. The calcined clay had a specific surface area of 29.6 m^2/g and a $D_{v,50}$ value of ~13 μm, see Table S3. As previously shown for the PC-52.5 paste, the addition of TIPA to LC^3-SP1 did not significantly alter the induction period neither the alite peak. However, TIPA clearly sharpens the aluminate peak. Furthermore, the C-S-H seeding admixtures slightly (and further) reduced the induction period. The influence of XS130 and STE53 on the alite peak is minor but on the aluminate peak is much larger. Both C-S-H based products boost aluminate hydration which is commonly followed by a sharp decrease in the released heat. This signature is widely observed and it has been mainly assigned to a slowdown of alite hydration because of the enhanced content of aluminate species in the pore solution [26]. The cumulative heat curves, see Fig. 2e, show a moderate increase of the heat evolved at seven days, the increase is much more notorious at 12 h.

Fig. 2c and f show the corresponding data for the SP2-processed LC^3 pastes. The reference paste, without any accelerating admixture, showed the alite and aluminate peaks at 5.1 and 13.2 h, respectively. The

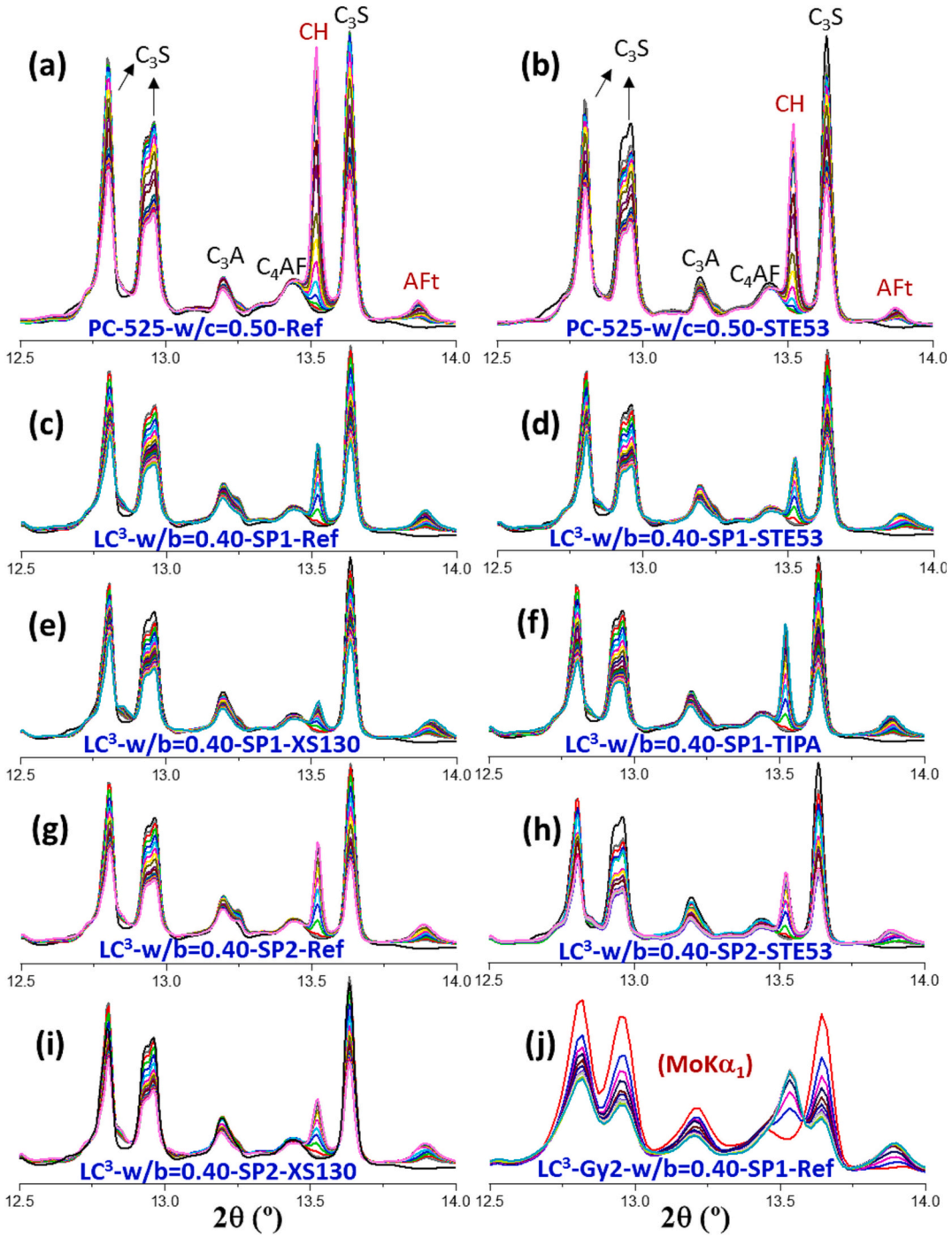

Fig. 3. Selected region of the raw *in situ* SXRPD patterns, λ = 0.62 Å, for the different pastes showing the dissolution of the clinker phases and the crystallisation of portlandite and ettringite during the first 24 h of hydration. The main diffraction peaks are marked according to the cement nomenclature. PC-52.5 series, panels (a) and (b). LC^3-SP1 series, panels (c) to (f). LC^3-SP2 series, panels (g) to (i). Panel (j) displays the *in situ* LXRPD patterns of LC^3-SP1-Ref-(Gy-2) series in which the x-axis (2θ/°) has been transformed to the synchrotron radiation for the sake of easy comparison.

behaviour of the pastes containing SP2 is quite similar to that shown by the pastes with SP1. Moreover, the role of the accelerating admixtures is totally in line with the changes discussed just above for the sister series containing SP1.

4.3. *In situ* synchrotron powder diffraction characterisation

4.3.1. *Initial discussion on the SXRPD direct results*

Two selected regions of the raw SXRPD patterns collected for the three studied series are displayed in Figs. 3 and 4. Fig. 3 allows us to directly follow, *i.e.* without any type of data treatment, the dissolution of the clinker phases and the crystallisation of portlandite and ettringite. Moreover, Fig. 4 directly displays the dissolution of gypsum and the appearance of ettringite and hemicarbonate. In detail, Fig. 3a and b show the selected regions of the patterns for PC-52.5-Ref and PC-52.5-STE53, respectively. Two main features deserve attention. Firstly, the admixture-containing paste shows an enhanced calcium aluminate hydration, both C_3A and C_4AF. Secondly, in spite of a similar C_3S dissolution rate, there is a lower rate of crystallisation of portlandite for PC-52.5-STE53, see Fig. 3b. This has been reported several times for C-S-H and alkanolamine activations [19,20,55,58,59], and it could be related to the C-S-H secondary nucleation. The C-S-H gel that preferably grows in the pore solution may have a larger Ca/Si ratio and hence, the corresponding portlandite amount would be smaller [59]. However, this hypothesis still lacks firm experimental confirmation. This will be the subject of further investigations.

Fig. 3c to f show the patterns for the LC^3 binder pastes with SP1. The evolution of the traces for LC^3-SP1-Ref compared to the PC-52.5-Ref indicates that C_3A reacts faster in the presence of the SCMs. Moreover, the amount of crystallising CH is very much reduced at 1 day which may indicate that the pozzolanic reaction is already taking place. Concerning the admixtures, STE53 and specially XS130 further reduce the amount of crystallising portlandite, see Fig. 3d and e, respectively. Conversely, TIPA, which does not significantly promote secondary C-S-H gel nucleation, and does not show a decreased portlandite crystallisation. In fact, slightly larger amounts of CH are inferred from the powder patterns. This can be due to the enhanced C_3S hydration and it will be discussed in the quantitative study, see below. Finally, Fig. 3g to i show the patterns for the LC^3 binder pastes with SP2. Note that TIPA paste in this series was not measured due to beamtime limitations. All the findings discussed above are again observed here. Especially, the C-S-H admixture containing pastes, *i.e.* LC^3-SP2-STE53 and LC^3-SP2-XS130, showed less portlandite than the reference paste, LC^3-SP2-Ref. A faster C_3A reactivity was again observed. In addition, Fig. 3j depicts the *in situ* laboratory powder patterns for LC^3-SP1-Ref-(Gy-2), for the sake of comparison, see below. As known, the powder diffraction peaks in the laboratory patterns are broader which results in larger peak overlapping.

Fig. 4a and b show alternative regions for PC-52.5-Ref and PC-52.5-STE53 patterns, respectively. For these binders, Hc does not precipitate, in the studied time range, and gypsum is fully dissolved. The remaining panels of Fig. 4 illustrate the evolution of the corresponding LC^3 binders without and with admixtures. It is evident that the admixtures accelerate Hc formation when compared to the reference LC^3 binders, see Fig. 4c and g. Moreover, for these LC^3 pastes, gypsum is not fully dissolved in the first day because of the large particle size of the additional gypsum dossaged to prepare these binders, *i.e.* $D_{v,50}$~33 μm.

4.3.2. *Quantitative analysis of the SXRPD data*

All collected SXRPD patterns have been analysed by the Rietveld method. The resulting values are deposited in the S.I., see Tables S6-S14. As examples of the obtained fits, Fig. S6 displays the Rietveld plots for the SXRPD patterns of PC-52.5-Ref-w/c = 0.50 and PC-52.5-STE53-w/c = 0.50 at 0.7 h of hydration; Fig. S7 shows the Rietveld plots for LC^3-SP1-Ref-w/b = 0.40 and LC^3-SP1-STE53-w/b = 0.40 at 11.2 h; and Fig. S8 reports the Rietveld plots for LC^3-SP2-Ref-w/b = 0.40 and LC^3-SP2-STE53-w/b = 0.40 at 19.4 h. In order to develop a unified picture, the phase contents are shown arranged as evolving phase (dissolution or crystallisation) rather than displaying the behaviour of the binders. The results for the analyses are displayed in Figs. 5–9. A discussion is carried out next to reveal the trends and to compare the behaviour of selected phases in different binders. In the next subsection, a more elaborated analysis is performed based on the equations given in the introduction. This is mainly carried out to estimate the MK degree of reaction in the investigated conditions.

Fig. 5 displays the hydration (dissolution) of alite and the concomitant crystallisation of portlandite. For PC-52.5-Ref, C_3S starts to significantly dissolve at ~3.5 h which is also the time when CH starts to be quantified. This behaviour fully agrees with the calorimetric study where the induction period ends approximately at 3 h, see Fig. 2a. STE53 enhances the C_3S dissolution at very early ages, 5 h or less, but lower amounts of CH are quantified at the same hydration age when compared to PC-52.5-Ref, see also Tables S6 and S7. As discussed above, this qualitative observation has been reported several times for C-S-H seeding [26] and it points towards the outer C-S-H, precipitating at very early ages in these conditions, having slightly larger Ca/Si ratios. Moreover, the addition of STE53 slightly reduces the dissolution rate of the C_3S hydration after 9–10 h, see Fig. 5a, when compared to the neat PC-52.5 paste. This could be caused by increased aluminate dissolution, see C_3A dissolution pattern below. Higher amounts of aluminate species in the pore solution are known to delay C-S-H growth [60–63] as well as C_3S dissolution.

Now, we focus on the alite dissolution in the corresponding LC^3 binders, see Fig. 5b and c. Firstly, alite starts to hydrate at ~2 h, much faster than in PC-52.5 pastes. This is very likely due to the filler effect [64] and it was also evidenced in the calorimetries. Secondly, the admixtures do not significantly accelerate the C_3S hydration in these LC^3 binders at very early ages, *i.e.* less than ~5 h. Thirdly, TIPA accelerates the hydration of C_3S after ~7 h for LC^3-SP1, see Fig. 5b. However, this is not observed in the calorimetric curve. Conversely, XS130 slightly delays C_3S hydration after ~7 h for this binder. The situation is very similar for the LC^3 binders with SP2, where neither STE53 nor XS130 seems to accelerate C_3S hydration, see Fig. 5c. Therefore, the increase in compressive strength at 1-day from LC^3-SP2 to LC^3-SP2-XS130 mortar, from 20 to 29 MPa (or 45 % gain) [35], is likely due to the secondary nucleation-growth effect with a much homogenous distribution of C-S-H and C-A-S-H gels. Similar strength gains are obtained by using STE53 admixture [36]. For this comparison, it is assumed that the degree of hydration of pastes and mortars are the same. Synchrotron X-ray diffraction tomography showed that C-S-H seeding partly moves the C-S-H gel regions away from the dissolving clinker particles towards the capillary porosity [65]. This rearrangement of the C-S-H gel, even for the same overall amount, yields a more homogeneous C-S-H distribution.

The most interesting and original result from this investigation is deduced from the portlandite content evolutions in the LC^3 binders. It can be seen that after about 7 h of hydration, the CH contents stagnate but C_3S keeps hydrating. This is a firm direct evidence that the pozzolanic reaction(s) starts as early as 7–9 h of hydration. This behaviour is observed for both families of pastes, containing both SP1 and SP2, see Fig. 5b and c, respectively. This will be further elaborated in the next subsection. Finally, it should be noted that CH content starts to stagnate at hydration times quite close to the aluminate peaks in the calorimetries, see Fig. 2b and c. This observation suggests that these aluminate peaks, in the heat flow traces for LC^3 binders, may have a contribution from the pozzolanic reaction.

Fig. 6 shows the dissolution of gypsum and the concomitant crystallisation of ettringite. We have chosen to represent the data in this way as sulfate availability is commonly the limiting reactant for AFt crystallisation. Aluminium could come from the dissolution of C_3A and C_4AF, as well as any amorphous aluminate phase(s). Moreover, MK is also a source of aluminium in the LC^3 binders. It can be seen that the amounts of $C\bar{S}H_2$ at very early hydration ages for PC-52.5-Ref and PC-

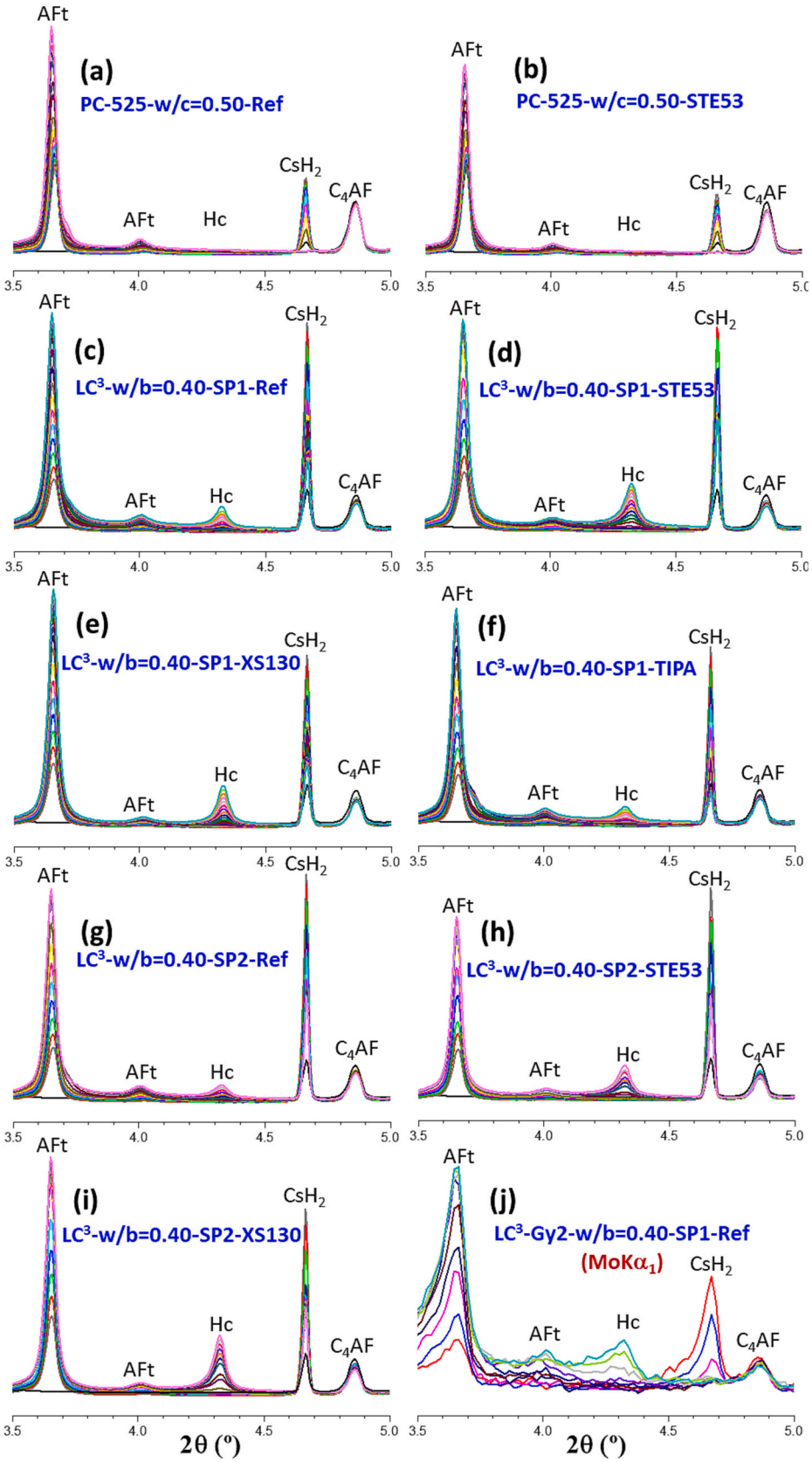

Fig. 4. Selected region of the raw *in situ* SXRPD patterns, λ = 0.62 Å, for the different pastes showing the dissolution of gypsum and the crystallisation of hemicarbonate and ettringite during the first 24 h of hydration. All details as in Fig. 3.

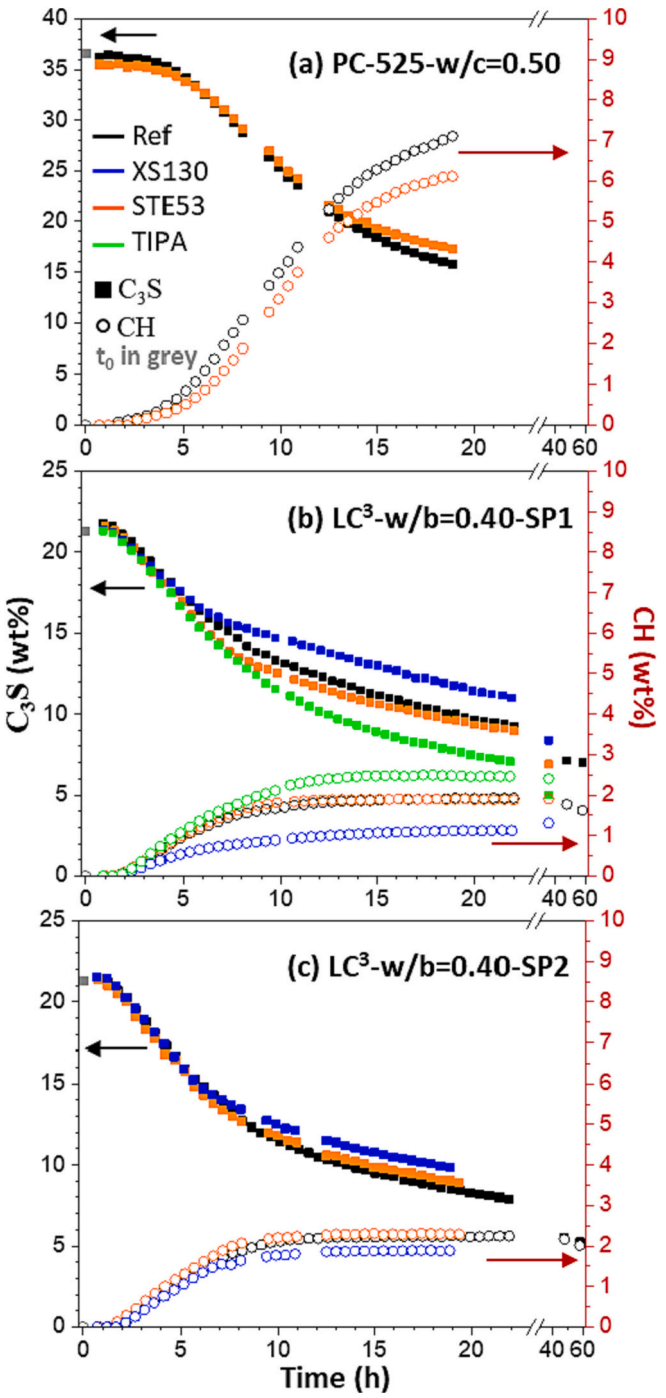

Fig. 5. Phase content evolutions with time from *in situ* SXRPD. (Left-axes) dissolution/hydration of alite. (Right-axes) crystallisation of portlandite. (a) PC-52.5 pastes which had w/c = 0.50. (b) LC^3-SP1 pastes, w/b = 0.40. (d) LC^3-SP2 pastes, w/b = 0.40. The symbols in grey colour indicate the starting amounts, *i.e.* $t = 0$.

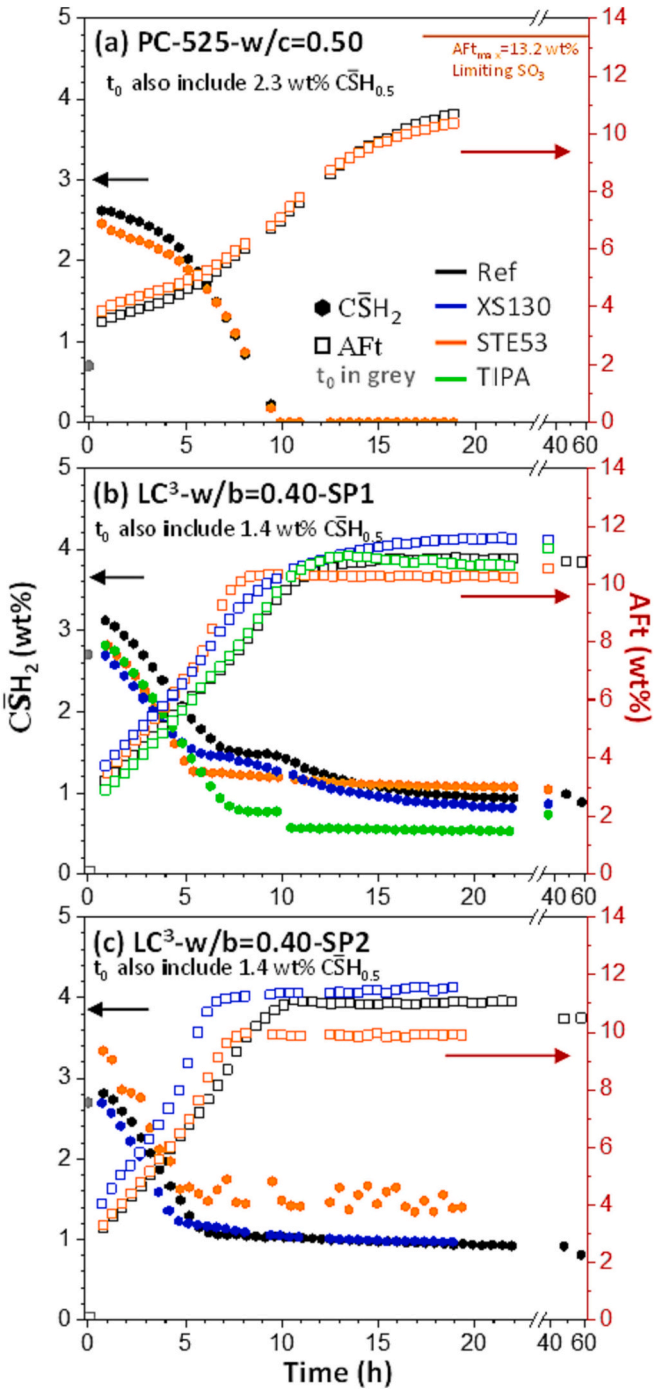

Fig. 6. Phase content evolutions as in Fig. 5. (Left-axes) dissolution of gypsum. (Right-axes) crystallisation of ettringite.

52.5-STE53 are invariably higher than at t_0. This has been previously observed, see for instance [19,63], and it is due to the fast dissolution of bassanite with the subsequent secondary gypsum crystallisation. The bassanite was present in the employed pristine cement, see Table S2. $C\bar{S}H_2$ fully dissolves at 10 h for PC-52.5-Ref and PC-52.5-STE53 but about 1 wt% remain undissolved for the LC^3 binders. This is due to the large particle size of the added gypsum, Gy-1, as will be demonstrated later.

Concerning the ettringite formation, AFt keeps crystallising beyond 10 h for PC-52.5-Ref and PC-52.5-STE53, *i.e.* when gypsum is fully dissolved. This indicates that there is an additional source of SO_4^{2-} anions, *i.e.* reservoir, which is likely the sulfate anions adsorbed on the C-S-H gel. Two features should be highlighted related to the AFt crystallisation. Firstly, the AFt crystallisation rate is much faster in LC^3 binders compared to the plain cement, see Fig. 6. The amount of AFt can be as high as 11.5 wt% as early as 7 h of hydration, see LC^3-SP2-XS130 in Fig. 6c. Secondly, the AFt contents stagnate at about 10–12 wt% for the LC^3 binders after 7–10 h of hydration. This is quite likely related to a lack of sulfates available for further crystallisation. The C-S-H seeding admixtures increased the amount of AFt at very early ages, before stagnation, but not the AFt amount at 20 h which is governed just by the

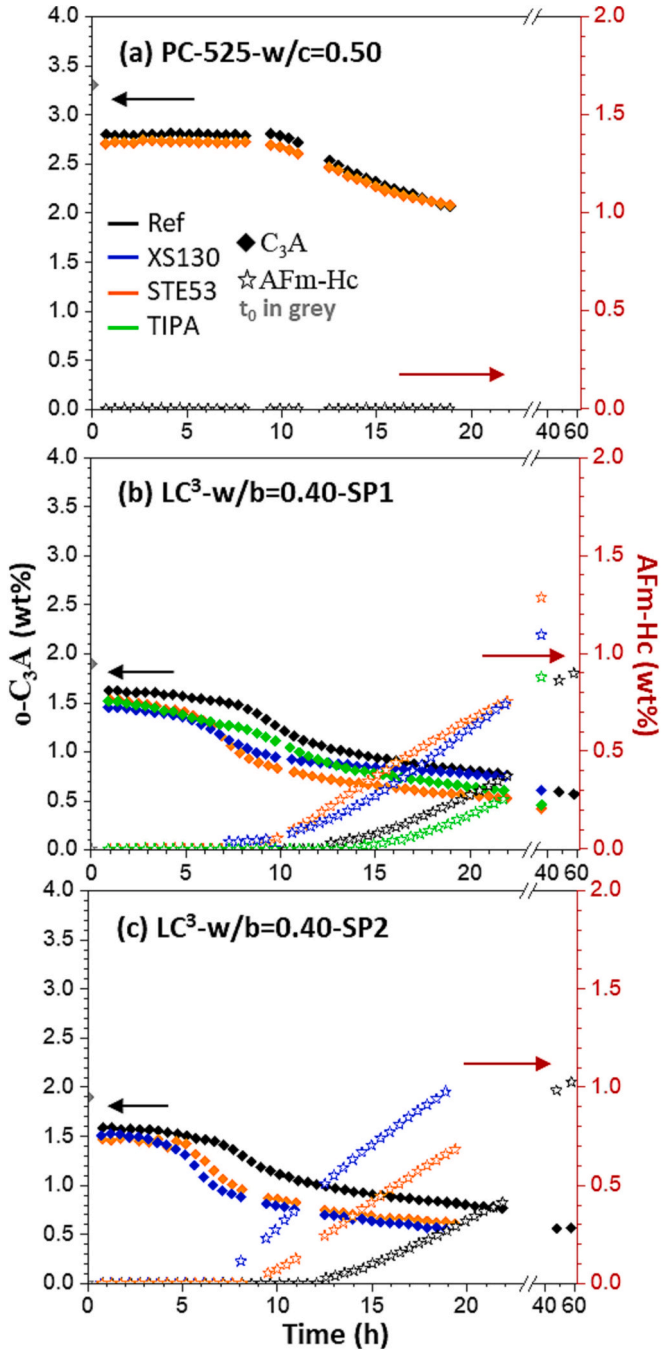

Fig. 7. Phase content evolutions as in Fig. 6. (Left-axes) hydration of tricalcium aluminate. (Right-axes) crystallisation of hemicarbonate.

sulfate availability. Fig. 7 displays both the hydration of tricalcium aluminate and the crystallisation of hemicarbonate. Hc only crystallises in the LC^3 system, *i.e.* it was not detected in PC-52.5-Ref and PC-52.5-STE53 pastes. For these pastes, C_3A started to hydrate at about 10 h, when $C\bar{S}H_2$ was fully dissolved. Furthermore, the enhancement of C_3A hydration by the STE53 admixture was not significant, see Fig. 7a. On the other hand, C_3A starts hydration much earlier in LC^3 binders, at 5 to 8 h of hydration. Moreover, C_3A hydration is strongly enhanced by the employed admixtures, see Fig. 7b and c. This is in agreement with the heat flow traces discussed earlier where the aluminate peaks were strongly enhanced. However, although there is an agreement in the heat flow, there is 1–2 h shift in the timing when the reaction happens.

It is worth noting that our data show that sulfates are adsorbed from

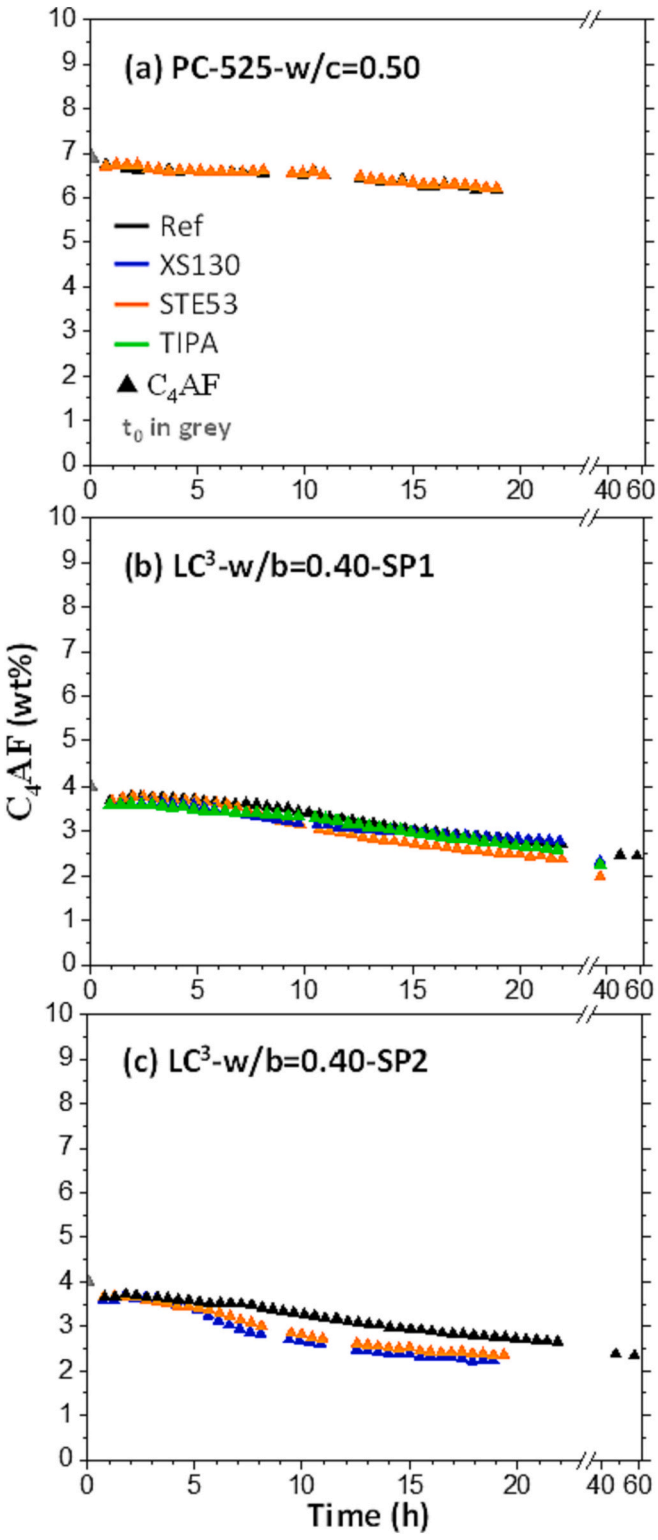

Fig. 8. Tetracalcium aluminoferrite content evolution as in Fig. 5.

C-S-H gel in the 10–20 h time interval for the PC pastes and in the 5–8 h interval for the LC^3 pastes, see Fig. 6. The roles of the SO_4^{2-} adsorption and desorption from C-S-H are difficult to discuss in the present investigation, beyond the obvious consequences in enhanced aluminate dissolution and ettringite precipitation. Comparing Figs. 5 and 6, there is not an acceleration in C_3S dissolution rate in these time intervals. We speculate that desorption of sulfate from C-S-H gel could result in faster C_3S dissolution because enhanced C-S-H growth rate. However, sulfate

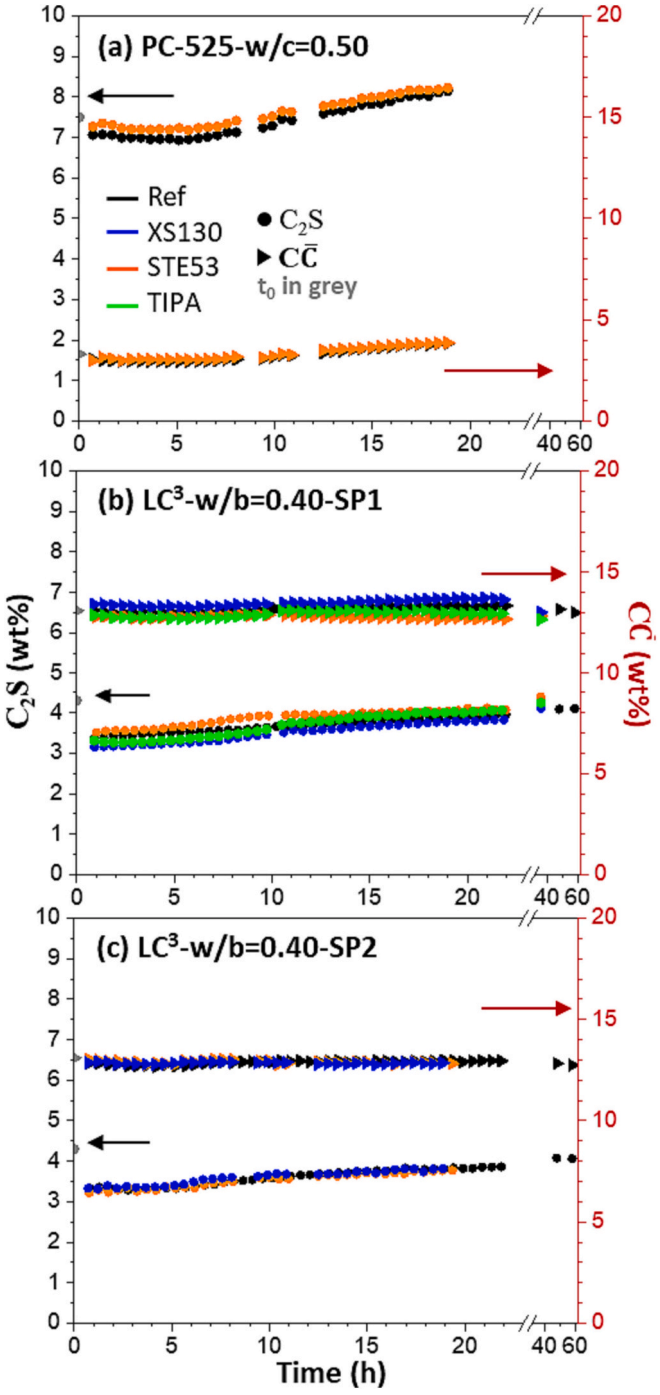

Fig. 9. Phase content evolutions as in Fig. 4. (Left-axes) belite results. (Right-axes) calcite results.

desorption from C-S-H also increases the dissolution rates of C_3A and C_4AF, and it is known that higher concentration of aluminates in the pore solution slows down the dissolution of alite. More research is needed, in properly designed experiments, to shed light on the consequences of sulfate desorption from C-S-H gel.

Another important and original result from this investigation is the Hc crystallisation in LC^3 binders. Hc crystallisation arises from any source of reactive alumina in presence of carbonate anions. We interpret the crystallisation of Hc as a second evidence of the pozzolanic reaction taking place at these ages, in addition to CH consumption, see above. This observation supports eqs. 4b or 4c, as the pozzolanic reaction has taken place for MK. Moreover, TIPA does not accelerate the Hc crystallisation but XS130 and STE53 do. TIPA seems to favour amorphous AFm precipitation. Comparing the C_3A dissolution and Hc crystallisation in Fig. 7b and c, it seems that SP2 has a synergistic effect with the C-S-H based admixtures resulting in enhanced C_3A dissolution and Hc crystallisation.

The amounts of Hc measured here, 0.3–1.0 wt% at 20 h and 0.9–1.3 wt% at 40 h (Tables S8-S14), are compared to those reported in bibliography next. These values are referred to 100 g of paste and the corresponding values referred to 100 g of anhydrous binder are 0.4–1.4 and 1.3–1.8 wt%, respectively. The accompanying AFt contents ranged 10–12 wt%, or 14–17 wt% when they are referred to 100 g of binder. Moreover, it must be noted that already in 2018 [66] it was demonstrated that carboaluminate contents are strongly dependent on the amount of MK in the calcined clay. Therefore, the comparison here is restricted to LC^3 binders with MK content 60–75 wt% and w/b = 0.40. Avet et al. [66] reported (Hc + Mc) amounts of ~0.8 and ~ 6.0 wt% at 1 and 3 d, respectively. The AFt content was 12.5 wt% at both ages. Zunino and Scrivener [67] reported (Hc + Mc) amounts of ~1.0 and 2.5 wt% at 1 and 2 d, respectively, with an associated AFt content of 8.5 wt % which increased to 10.0 wt% at 2 d. Finally, larger values were reported in [68]. For the binder with 3.6 wt% of SO_3, the reported amounts of (Hc + Mc) and AFt at 3 days were 9.8 and 17.0 wt%, respectively.

Fig. 8 shows the hydration of C_4AF. On the one hand, C_4AF hydrates very little in the measured time range for PC-52.5, see Fig. 8a. STE53 does not seem to modify C_4AF hydration in the PC-52.5 pastes. On the other hand, C_4AF is more reactive in LC^3 binders. The studied admixtures modestly accelerate the C_4AF hydration in LC^3-SP1 binders. Conversely, XS130 and STE53 accelerated the C_4AF hydration more significantly when the pastes contained SP2. The understanding of this synergistic effect, also found in C_3A hydration, see just above, requires further investigations.

Fig. 9 displays the time evolution of C_2S and $C\bar{C}$. During the studied time range, the dissolution of these phases could not be evidenced. The plots show constant values within the variability and accuracy of the analyses. It is noted that the maximum amount of measured Hc, 1.4 g, requires the dissolution of 0.12 g of $C\bar{C}$, both values referred to 100 g of paste. The quantification of the dissolution of 0.12 wt% of $C\bar{C}$ is not reliably attained even by synchrotron powder diffraction.

The degree of hydration (DoH) of the clinker phases can be directly determined from the data reported in Tables S6-S14, as the mineralogical analyses are always referred to 100 g of paste. This can be done because of the use of the internal standard, see experimental section. Thus, Fig. 10(a) displays the DoH for the PC-52.5-Ref and PC-52.5-STE53 series. It can be seen that the DoH of C_3S is about 30 % at ~10 h, *i.e.* the maximum of the heat flow peak, and about 55 % at 19 h, *i.e.* the time for the aluminate peak. At this age, 19 h, the hydration degree of C_4AF is still quite small, ~10 %, but that of C_3A is ~35 % and ramping up. It can also be seen that the employed admixture marginally modifies the DoH of these phases for this highly reactive cement. C_3S hydration is slightly decelerated after 14 h, see Fig. 10(a).

Fig. 10(b) and (c) display the DoH for the clinker phases for the LC^3-SP1 and LC^3-SP2 series, respectively. The following observations can be extracted from these plots: (i) C_3S hydration is accelerated by the presence of the SCMs. The 30 % DoH is reached at ~10, ~7.5 and ~ 6 h for PC-52.5-Ref, LC^3-Ref-SP1 and LC^3-Ref-SP2. This is likely due to the filler effect, although it should be kept in mind that the C_3S-water ratios are different in the two series. It must also be noted that the LC^3 series have SP which could delay C_3S hydration but it does not seem to counterbalance the filler effect. As expected, this enhanced reaction is damped at later ages, after about 18 h. (ii) C_4AF hydration rate is highly enhanced in LC^3 binders. For instance, C_4AF DoHs at 19 h are 10, 31 and 32 % for PC-52.5-Ref, LC^3-Ref-SP1 and LC^3-Ref-SP2, respectively. (iii) C-S-H nucleation seeding admixtures are very effective in boosting C_4AF hydration in LC^3 binders, see Fig. 10(b) and (c). For instance, the DoH of

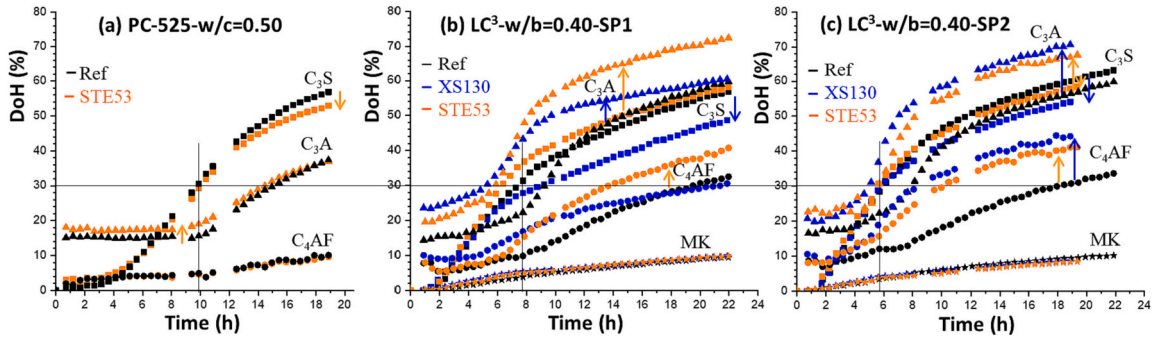

Fig. 10. Degree of hydration of the clinker phases and metakaolin as a function of time. (a) Data for the PC-52.5 series where the influence of the STE53 admixture is also shown. (b) Data for the LC^3-SP1 series where both studied admixtures (STE53 and XS130) accelerate the hydration of C_3A and C_4AF. C_3S hydration is slightly decelerated at later ages by XS130. (c) Data for the LC^3-SP2 series displaying a similar behaviour than that of LC^3-SP1. Metakaolin hydration is not significantly boosted by the employed admixtures up to 1 day.

C_4AF at 20 h increases from 30 % for the reference paste to ~40 % for the two pastes containing STE53 admixture. (iv) C_3A also hydrates faster in LC^3 binders than in the plain PC, see Fig. 10. C_3A DoHs at 19 h are ~36, ~56 and ~ 57 % for PC-52.5-Ref, LC^3-Ref-SP1 and LC^3-Ref-SP2, respectively. (v) The employed admixtures are also very effective in boosting C_3A hydration in LC^3 binders, especially STE53, see Fig. 10(b) and (c). The DoH of C_3A at 19 h increases from 56 and 57 % for the reference pastes SP1 and SP2, to 70 and 68 % for the corresponding pastes containing STE53. (vi) The employed admixtures also slightly deaccelerate C_3S hydration at later ages in the studied LC^3 binders. The exception is STE53 in LC^3-SP1 where the C_3S rate of hydration is slightly enhanced. A similar overall behaviour is shown by TIPA and the corresponding traces are shown in Fig. S9(a). They are not included in Fig. 10 for the sake of clarity.

To end this subsection, the DoH of MK is also displayed in Fig. 10(b) and (c). The calculation to obtain these values is detailed in the next section, but the results are reported here for completeness. The estimated degree of hydration is close to 10 % at 1 day and it does not seem to be significantly enhanced by the employed admixtures in the studied time interval.

4.3.3. *Hydration reaction discussion including mass balance calculations*

The calculated amounts of hydrated phases were obtained by the hydration eqs. [42] given in the annex and the mass-balance calculations. The steps for the calculations are graphically shown in Fig. 11, which are based on previous publications for LC^3 systems [41,68,69] but simplified for accounting the reactions just taking place during the first day of hydration. For instance, it does consider the formation of monocarboaluminate. It is noted that the employed cement has relatively low magnesium content, 1.5 wt%, and the formation of amorphous hydrotalcite has also not been considered here.

Step (1). The reacted crystalline C_4AF fraction is computed according to eq. 3a. This yields calculated amounts of amorphous siliceous hydrogarnet $C_3FS_{0.84}H_{4.32}$, AFt and CH. Additionally, the required amount of C_3S is subtracted from the total reacted amount of C_3S.

Step (2). The reacted crystalline C_3A fraction is computed according to eq. 2. This yields a calculated value of AFt which is added to the one resulting from C_4AF hydration.

Step (3). The reacted C_3S content, after subtraction of the C_3S required for eq. 3a, is computed according to eq. 1. This yields calculated amounts of C-S-H and CH. A (very minor) correction factor, 98 %,

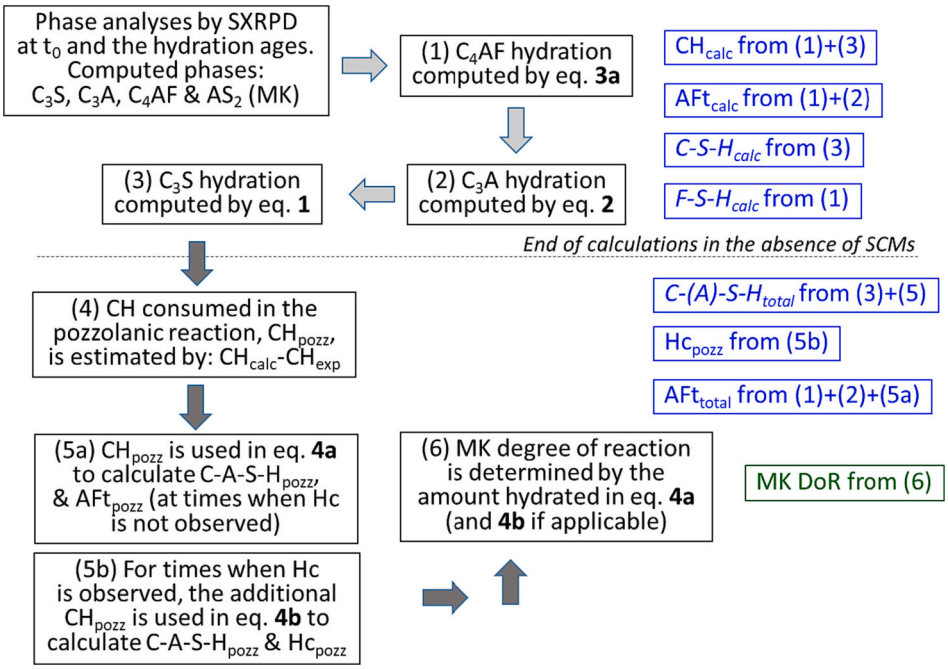

Fig. 11. Flowchart with the steps followed for the calculations of the hydrated phases including the determination of the degree of reaction of metakaolin in LC^3 binders by mass balance.

is applied to the obtained CH amount to account for the released magnesium which does not form crystalline portlandite. The total amount of CH is obtained by adding the small amount from step (1) and the much larger amount from step (3).

In the absence of metakaolin, the calculations stop here. For the LC^3 binders, in addition of the three steps described above, the following steps are also followed.

Step (4). The consumed CH in the pozzolanic reaction, labelled CH_{pozz}, is obtained as the subtraction of CH_{calc} and the measured amount of portlandite, CH_{exp}.

Step (5a). If Hc is not detected, CH_{pozz} is used according to eq. 4a to calculate the amounts of C-A-S-H_{pozz} and AFt_{pozz}. AFt_{total} is computed as the sum of AFt_{calc} and AFt_{pozz}.

Step (5b). For times when Hc is experimentally detected, the additional CH_{pozz} is used according to eq. 4b to calculate C-A-S-H_{pozz} and Hc.

Step (6). Calculates the degree of reaction of MK from the amount of MK at t_0 and the amount consumed by eq. 4a (and 4b if applicable) at a given age.

Following this approach, Fig. 12 displays the comparison between the measured and calculated amounts of portlandite. On the one hand, the evolution of calculated portlandite fractions for PC-52.5-w/c = 0.50 series show the same pattern than the experimental ones, see Fig. 12(a). It must be noted that the model calculates about 0.5–0.8 wt% more CH at later ages than the measured ones. This disagreement could be due to experimental inaccuracies and also to the initial formation of a minor amount of amorphous $Ca(OH)_2$. This fraction of amorphous calcium hydroxide could be intermixed with (and/or adsorbed at) C-S-H slightly increasing the C/S ratio above the assumed 1.8 value [59,70]. On the other hand, the dilution of 50 % in the clinker should decrease the amount of portlandite roughly by 50 %, *i.e.* from 8 to 4 wt%, for the LC^3 binders. In fact, the calculate amounts of CH at 20 h in the LC^3-Ref pastes are slightly higher than 4 % because the (above discussed) filler effect, see Fig. 12(b) and (c). Very importantly, the measured amount of CH after 7–8 h stagnates between 1.3 and 2.1 wt%. This is about half of the CH that should be produced by the measured C_3S hydration, *i.e.* CH_{calc}, and a firm prove that pozzolanic reaction is taken place as early as 7–8 h after water mixing. Moreover, as it is highlighted by lines in Fig. 12(b) and (c), the rate of growth of CH_{exp} in LC^3 systems at times earlier than 7 h (solid lines) is smaller than that of CH_{calc} (dashed lines) which suggest that pozzolanic reaction is taken place at even earlier ages.

Fig. 13 displays the comparison between the measured and calculated amounts of crystalline ettringite for the three studied series. This is the weakest point of this work as the disagreement is large, the biggest being 3.2 wt% at 11 h for PC-52.5-Ref. Fig. 13a shows the results for the PC-52.5-w/c = 0.50 pastes where the experimentally measured amounts of AFt are 1–3 wt% larger than the calculated ones, which are based on the dissolution of the crystalline aluminates within the pristine cement. The possible origins of this disagreement are elaborated next and they highlight the limitations of powder diffraction where some assumption have to be carried out in the data analysis. On the one hand, the measured amount of AFt could be overestimated because experimental inaccuracies. In this sense, preferred orientation of ettringite crystals was checked and it was not present. However, iron can replace aluminium in AFt and this is not considered in the Rietveld fits. If there is a significant amount of Fe within the ettringite crystal structure, this phase contains more electrons and therefore it diffracts more. Hence, a higher scale factor for pure-Al AFt is needed in the Rietveld fit, which directly translates to higher amount of this phase. On the other hand, the amount of calculated AFt can be underestimated in our methodology. We speculate that the two largest contributions to this possible underestimation are the presence of amorphous calcium aluminate(s) within the pristine cement and the assumed Al/Fe ratio in C_4AF, *i.e.* 1.0. It has been very recently demonstrated that C_4AF can be aluminium-rich [59] leading to higher AFt crystallisation. Amorphous calcium aluminates would dissolve leading to additional (non calculated) ettringite. In order to establish a limit, under the assumption that the total discrepancy is due to amorphous calcium aluminates, 3.2 wt% of AFt would require the dissolution of 0.7 wt% of amorphous C_3A in the paste, which is equivalent to 1.0 wt% in the pristine cement.

Concerning the LC^3-w/b = 0.40 series, it is important to note that the measured amount of AFt is similar to that of the neat PC, *i.e.* about 11 wt % referred to 100 g of paste, see Fig. 13(b) and (c); in spite of having half of the clinker. This is due to the enhanced reactivities of C_3A and C_4AF at early ages in LC^3 binders. The disagreement between calculated AFt amounts (from crystalline C_3A and C_4AF) and the experimentally measured fractions is also observed but quantitatively much smaller, *i.e.* ~1.5 wt%. This is considered within the errors due to the experimental inaccuracies and the assumptions in the calculations. Moreover, after about 9–10 h, AFt stagnates as available sulfates are depleted. As C_3A and C_4AF keep dissolving, AFt_{total} continues to increase but the aluminates are mainly employed in the Hc crystallisation see just below.

It should be noted that the AFt crystallisation in OPC and LC^3 binders show quite different behaviours. The crystallisation of AFt is still taking place at 20 h for PC-525-w/c = 0.50 series, but it stagnates at about 10 h in the LC^3 pastes. This is due to the different sulfate requirements and availabilities. On the one hand, the original PC has 3.8 wt% of SO_3, leading to 2.53 wt% in the paste and therefore, it may develop a maximum of 13.2 g of AFt (referred to 100 g of paste). The largest AFt amount measured for these pastes is 11.0 wt%, and hence, sulfates are not depleted at the latest measured age. On the one hand, the LC^3 binder pastes have a total available SO_3 content of ~1.94 wt% (1.32 from the PC and ~ 0.62 from the added gypsum taking into account the undissolved fraction). This SO_3 value leads to a maximum AFt content of 10.2 wt%, which agrees reasonably well with the measured amounts of

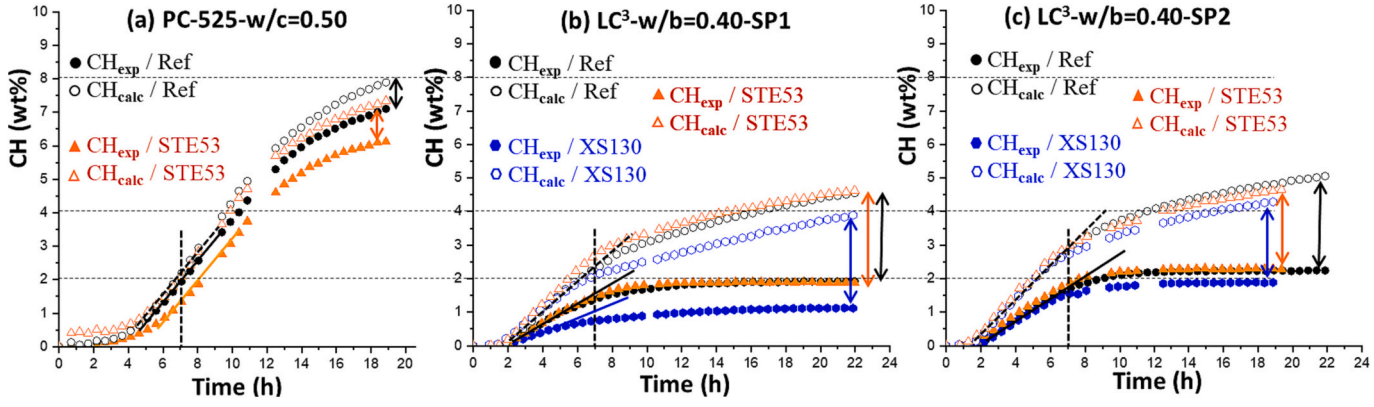

Fig. 12. Experimental (solid symbols) and calculated (open symbols) amounts of portlandite as a function of the hydration time for (a) PC-52.5-w/c = 0.50 series, (b) LC^3-w/b = 0.40-SP1 series and (c) LC^3-w/b = 0.40-SP2 series. The dashed lines at 2.0, 4.0 and 8.0 wt% of CH are guides to the eyes. For the discussion of the other lines, see the text.

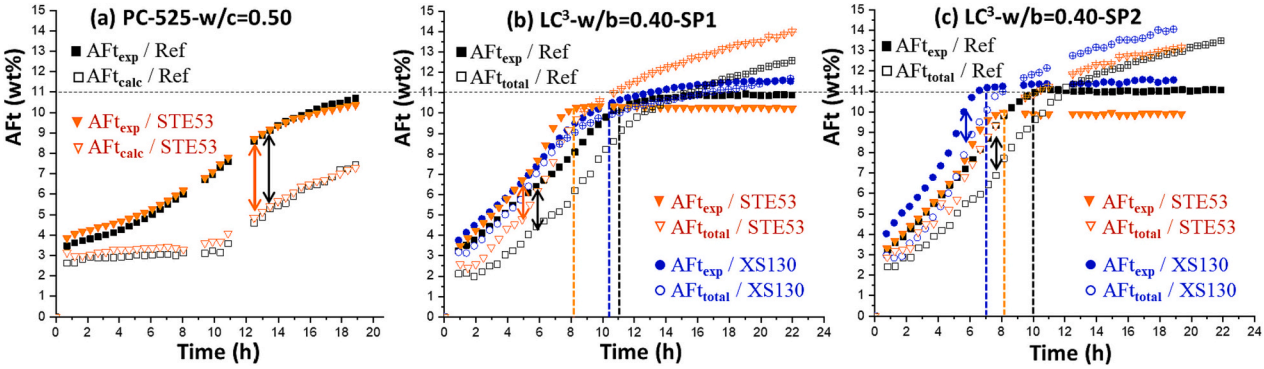

Fig. 13. Experimental (solid symbols) and calculated (open symbols from eq. 4a and crossed out when eq. 4b was used) amounts of crystalline ettringite as function of the hydration time for (a) PC-52.5-w/c = 0.50 series, (b) LC^3-w/b = 0.40-SP1 series and (c) LC^3-w/b = 0.40-SP2 series. The horizontal dashed line at 11.0 wt% of AFt is a guide to the eyes. The times of stagnation of AFt crystallisation are highlighted by vertical dashed lines. The double arrows mark the discrepancy between calculated and measured total amounts of AFt.

ettringite at the stagnation points. Clearly, for these LC^3 systems and at about 8–10 h, the sulfates are depleted from the pore solution which agrees very well with the aluminate peak in the calorimetries, see Fig. 2b and c. Moreover, the AFt crystallisation rates are also different in PC and LC^3 pastes, see Fig. 13. AFt measured crystallisation rate for LC^3 pastes is much faster than that in PC because the previously discussed enhanced dissolution rates of C_3A and C_4AF.

As expected, Hc_{exp} starts to appear when the AFt content stagnates, see Fig. 13 and 14. The agreement between Hc_{exp} and Hc_{pozz} precipitation rates, see Fig. 14, is acceptable with errors lower than 0.5–0.6 wt %.

The corresponding plots with the comparison of experimental and calculated amounts of hydrates for TIPA admixture in the series LC^3-SP1 are given in Fig. S9. Moreover, the calculated amounts of amorphous phases are also deposited, see Fig. S10.

Finally, these hydration reactions and the associated mass balance calculation allow us to estimate the DoH of MK. The raw clay had ~74 wt% of kaolinite which means a ~ 71 wt% of MK in the calcined clay employed to prepare the LC^3 binders. As the calcined clay was added at 30 % and then diluted to a w/b = 0.40, the MK content at t_0 in the pastes was 15.2 wt%. Now, it is possible to determine the MK DoH with the consumed $Ca(OH)_2$ values, *i.e.* CH_{pozz}, under the assumptions stated above. The DoH of MK at 22 h in these LC^3 systems is ~10 %, see Fig. 10 (b) and (c). This calculation sets a minimum value for the degree of reaction of MK, which could be slightly larger as it is known the MK also partly reacts with the amorphous $Ca(OH)_2$ of the C-S-H gel leading to overall smaller values of C/S ratio in both C-S-H and C-A-S-H gels [71,72].

Interestingly, this calculation shows that for a LC^3–50 cement with 71 wt% of MK, where 60 % of alite is already hydrated, just 10 % MK was consumed and there was CH left for the reaction of a further 10 %, see Fig. 12(b) and (c). This means that for a typical DoH of 90 % of alite, there is portlandite for just the reaction of 30 % of the MK. This simple calculation shows that calcined clays with one-third of their kaolinite content, *i.e.* ~30 wt%, have the potential to exhaust all portlandite from alite hydration in LC^3–50 binders at later ages. This may justify that calcined clays with modest MK contents, *i.e.* 30–40 wt%, yields relatively competitive late strengths; however, at early ages calcined clays with larger amounts of MK yield higher strengths.

4.4. *In situ laboratory powder diffraction characterisation*

This study was motivated by the observation of ~1 wt% of undissolved gypsum after about 10 h of hydration in the LC^3 pastes. Fig. 15 shows the *in situ* synchrotron and laboratory powder patterns for LC^3-SP1-Ref fabricated with Gy-1. Furthermore, Fig. 15 also displays the corresponding *in situ* laboratory powder patterns for the same binder but fabricated with Gy-2 which has a smaller average particle size, see experimental section. This study reproduces the lack of complete dissolution of the gypsum with large particle sizes, see Fig. 15b. Conversely, gypsum with smaller particle sizes, *i.e.* Gy-2, is fully dissolved after 14 h in the LC^3 binder, see Fig. 15c. This observation demonstrates the robustness of the experimental procedures and it highlights the (overlooked) importance of having relatively small

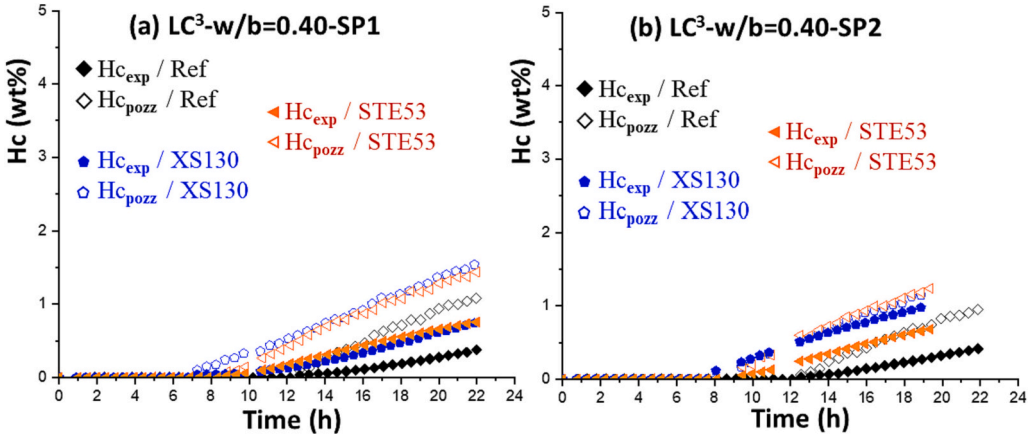

Fig. 14. Experimental (solid symbols) and calculated (open symbols) amounts of crystalline hemicarbonate as a function of the hydration time for (a) LC^3-w/b = 0.40-SP1 and (b) LC^3-w/b = 0.40-SP2.

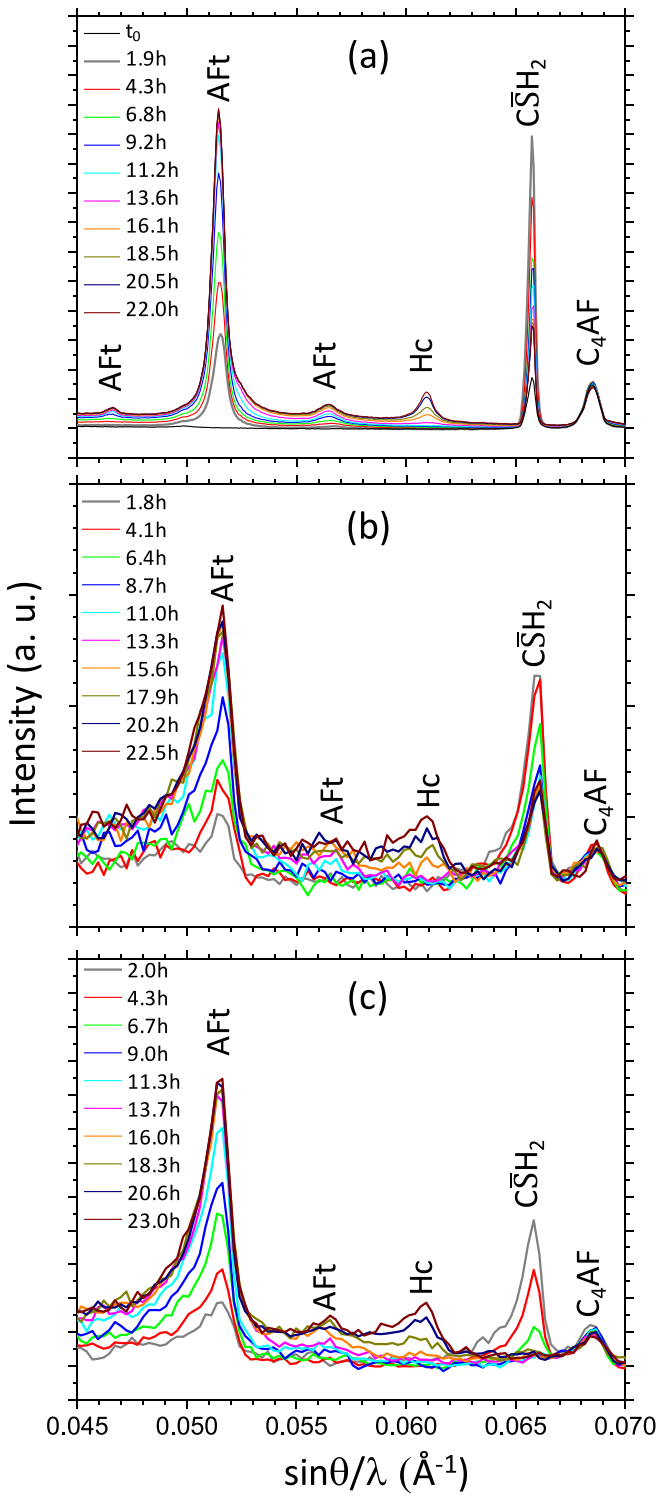

Fig. 15. Selected view for the raw patterns for the LC^3-SP1-Ref pastes during the first day of hydration. The main diffraction peaks are labelled. (a) SXRPD data, λ = 0.62 Å, for LC^3-SP1-Ref fabricated with Gy-1. (b) LXRPD data, λ = 0.71 Å, for LC^3-SP1-Ref prepared with Gy-1. (c) LXRPD data, λ = 0.71 Å, for LC^3-SP1-Ref prepared with Gy-2.

particle sizes even for quite soluble phases.

A Rietveld quantitative study has also been carried out for the *in situ* laboratory X-ray powder patterns. The direct Rietveld results are deposited in Tables S15 and S16 for Gy-1 and Gy-2 samples, respectively. Hence, any interested reader could see the results but we do not discuss them here as they are in line with the SXRPD values, and they inherently have larger errors.

5. Conclusions

Four main conclusions can be drawn from the present investigation dealing with the early hydration of LC^3–50 pastes by *in situ* synchrotron X-ray powder diffraction.

Firstly, for LC^3 pastes, fabricated with a calcined clay with ~71 w% of MK, the pozzolanic reaction starts as early as 7 h. This is shown by the consumption of portlandite, as alite keeps dissolving but additional crystalline $Ca(OH)_2$ is not formed.

Secondly, the hydration rates of the clinker phases in LC^3 binders are accelerated at very early ages, 3–10 h, by the presence of the supplementary materials which had fine particle sizes and high BET-surfaces. This has been reported previously and it is a clear sign of the filler effect.

Thirdly, the use of the employed C-S-H nucleation seeding admixtures, STE53 and XS130, enhanced the hydration rates of the calcium aluminate phases, both C_3A and C_4AF, in LC^3 binders. These admixtures also seem to partly change the alite hydration mechanism moving the C-S-H gel towards the pore solution but this cannot be directly measured by diffraction techniques.

Finally, the degree of hydration of metakaolin has been estimated, 10 % at 22 h, based on the pozzolanic reaction which gave the best agreement between the measured and calculated crystalline hydrated product contents.

CRediT authorship contribution statement

Alejandro Morales-Cantero: Data curation, Formal analysis, Investigation, Methodology, Resources, Software, Writing – original draft, Writing – review & editing. **Angeles G. De la Torre:** Formal analysis, Investigation, Writing – original draft, Writing – review & editing. **Ana Cuesta:** Formal analysis, Investigation, Writing – original draft, Writing – review & editing. **Isabel Santacruz:** Formal analysis, Investigation, Writing – review & editing. **Isabel M.R. Bernal:** Formal analysis, Investigation, Writing – review & editing. **Oliver Mazanec:** Formal analysis, Investigation, Writing – review & editing. **Alessandro Dalla-Libera:** Formal analysis, Investigation, Writing – review & editing. **Pere Borralleras:** Formal analysis, Investigation, Writing – review & editing. **Miguel A.G. Aranda:** Conceptualization, Formal analysis, Investigation, Supervision, Writing – original draft, Writing – review & editing.

Declaration of competing interest

Master Builders Solutions has a research contract, "Low-CO2 cement admixture activation study", with the research group of University of Malaga. However, the company has not issued any guidelines for the analysis or reporting of the data. The raw data have been openly deposited at zenodo.

Data availability

Synchrotron X-ray powder diffraction, laboratory X-ray powder diffraction and isothermal calorimetry raw data are available on Zenodo at doi:https://doi.org/10.5281/zenodo.7761337, and they can be used under the Creative Commons Attribution licence. Full details concerning the datasets are given in the Supplementary Information.

Acknowledgement

This research was partly supported by the research grant PID2020-114650RB-I00 which is co-funded by ERDF. ALBA synchrotron is thanked for providing beamtime at the BL04-MSPD beamline. We thank thorough discussions with Peter Schwesig and Sebastien Dhers from

Master Builders Solutions. Funding for open access charge: Universidad de Malaga/CBUA

Appendix A. Hydration reactions for the mass balance calculations

Table A1
Model clinker phase hydration reactions. The equation (eq.) number is given in the right column.

Clinker phase hydration reaction	Eq.
$Ca_3SiO_5 + 5.2H_2O \rightarrow 1.2Ca(OH)_2 + (CaO)_{1.8}SiO_2(H_2O)_{4.0}$	(1)
$Ca_3Al_2O_6 + 3CaSO_4{\cdot}2H_2O + 26H_2O \rightarrow Ca_6Al_2(SO_4)_3(OH)_{12}{\cdot}26H_2O$	(2)
$Ca_4Al_2Fe_2O_{10} + 0.84Ca_3SiO_5 + 3CaSO_4{\cdot}2H_2O + 30.84H_2O \rightarrow Ca_3Fe_2(SiO_4)_{0.84}(OH)_{8.64} + Ca_6Al_2(SO_4)_3(OH)_{12}{\cdot}26H_2O + 0.52Ca(OH)_2$	(3a)
$Ca_4Al_2Fe_2O_{10} + 1.68Ca_3SiO_5 + 11.68H_2O \rightarrow 2Ca_3FeAl(SiO_4)_{0.84}(OH)_{8.64} + 3.04Ca(OH)_2$	(3b)

Table A2
Model pozzolanic hydration reactions.

Pozzolanic hydration reaction	Eq.
$Al_2Si_2O_7 + 5.4Ca(OH)_2 + 2.4CaSO_4{\cdot}2H_2O + 23.4H_2O \rightarrow 2Ca_{1.5}Al_{0.2}SiO_{3.8}(H_2O)_{4.0} + 0.8Ca_6Al_2(SO_4)_3(OH)_{12}26H_2O$	(4a)
$Al_2Si_2O_7 + 5.8Ca(OH)_2 + 0.4CaCO_3 + 11.8H_2O \rightarrow 2Ca_{1.5}Al_{0.2}SiO_{3.8}(H_2O)_{4.0} + 0.8Ca_4Al_2(OH)_{13}(CO_3)_{0.5}(H_2O)_{5.5}$	(4b)
$Al_2Si_2O_7 + 5.6Ca(OH)_2 + 0.2CaCO_3 + 1.2CaSO_4{\cdot}2H_2O + 17.6H_2O \rightarrow 2Ca_{1.5}Al_{0.2}SiO_{3.8}(H_2O)_{4.0} + 0.4Ca_4Al_2(OH)_{13}(CO_3)_{0.5}(H_2O)_{5.5} + 0.4Ca_6Al_2(SO_4)_3(OH)_{12}26H_2O$	(4c)
$Al_2Si_2O_7 + 5.4Ca(OH)_2 + 0.8CaCO_3 + 7.4H_2O \rightarrow 2Ca_{1.5}Al_{0.2}SiO_{3.8}(H_2O)_{4.0} + 0.8Ca_4Al_2(OH)_{12}(CO_3)(H_2O)_5$	(5)

Appendix B. Supplementary data

Supplementary data to this article can be found online at https://doi.org/10.1016/j.cemconres.2024.107463.

References

[1] IEA, Global energy and CO2 emissions in 2020 – Global Energy Review 2020 – Analysis - IEA. https://www.iea.org/reports/global-energy-review-2020/global-energy-and-co2-emissions-in-2020, 2020 (accessed May 13, 2023).

[2] H.F.W. Taylor, Cement Chemistry, 2nd ed., Thomas Telford Pub, London, UK, 1997.

[3] W.B.C. for Sustainable Development, Cement Sustainability Initiative. Cement Industry Energy and CO2 Performance "Getting the Numbers Right,", Cem. Sustain. Initiat. (2009). http://docs.wbcsd.org/2009/06/CementIndustryEnergyAndCO2Performance.pdf.

[4] G. Habert, S.A. Miller, V.M. John, J.L. Provis, A. Favier, A. Horvath, K.L. Scrivener, Environmental impacts and decarbonization strategies in the cement and concrete industries, Nat. Rev. Earth Environ. 1 (2020) 559–573, https://doi.org/10.1038/s43017-020-0093-3.

[5] C. Shi, B. Qu, J.L. Provis, Recent progress in low-carbon binders, Cem. Concr. Res. 122 (2019) 227–250, https://doi.org/10.1016/j.cemconres.2019.05.009.

[6] UN Environment, K.L. Scrivener, V.M. John, E. Gartner, Eco-efficient cements: potential, economically viable solutions for a low-CO2, cement-based materials industry, Cem. Concr. Res. 114 (2018) 2–26. doi:https://doi.org/10.1016/j.cemconres.2018.03.015.

[7] L. Barcelo, J. Kline, G. Walenta, E. Gartner, Cement and carbon emissions, Mater. Struct. 47 (2014) 1055–1065, https://doi.org/10.1617/s11527-013-0114-5.

[8] S.J. Davis, N.S. Lewis, M. Shaner, S. Aggarwal, D. Arent, I.L. Azevedo, S.M. Benson, T. Bradley, J. Brouwer, Y.M. Chiang, C.T.M. Clack, A. Cohen, S. Doig, J. Edmonds, P. Fennell, C.B. Field, B. Hannegan, B.M. Hodge, M.I. Hoffert, E. Ingersoll, P. Jaramillo, K.S. Lackner, K.J. Mach, M. Mastrandrea, J. Ogden, P.F. Peterson, D. L. Sanchez, D. Sperling, J. Stagner, J.E. Trancik, C.J. Yang, K. Caldeira, Net-zero emissions energy systems, Science 360 (2018) eaas9793, https://doi.org/10.1126/science.aas9793.

[9] M.C.G. Juenger, R. Siddique, Recent advances in understanding the role of supplementary cementitious materials in concrete, Cem. Concr. Res. 78 (2015) 71–80, https://doi.org/10.1016/j.cemconres.2015.03.018.

[10] M.C.G. Juenger, R. Snellings, S.A. Bernal, Supplementary cementitious materials: new sources, characterization, and performance insights, Cem. Concr. Res. 122 (2019) 257–273, https://doi.org/10.1016/j.cemconres.2019.05.008.

[11] K.L. Scrivener, F. Martirena, S. Bishnoi, S. Maity, Calcined clay limestone cements (LC3), Cem. Concr. Res. 114 (2018) 49–56, https://doi.org/10.1016/j.cemconres.2017.08.017.

[12] M. Sharma, S. Bishnoi, F. Martirena, K. Scrivener, Limestone calcined clay cement and concrete: a state-of-the-art review, Cem. Concr. Res. 149 (2021) 106564, https://doi.org/10.1016/j.cemconres.2021.106564.

[13] T. Hanein, K.-C. Thienel, F. Zunino, A.T.M. Marsh, M. Maier, B. Wang, M. Canut, M.C.G. Juenger, M. Ben Haha, F. Avet, A. Parashar, L.A. Al-Jaberi, R.S. Almenares-Reyes, A. Alujas-Diaz, K.L. Scrivener, S.A. Bernal, J.L. Provis, T. Sui, S. Bishnoi, F. Martirena-Hernández, Clay calcination technology: state-of-the-art review by the RILEM TC 282-CCL, Mater. Struct. 55 (2021) 1–29, https://doi.org/10.1617/S11527-021-01807-6.

[14] R.J. Flatt, N. Roussel, C.R. Cheeseman, Concrete: an eco material that needs to be improved, J. Eur. Ceram. Soc. 32 (2012) 2787–2798, https://doi.org/10.1016/J.JEURCERAMSOC.2011.11.012.

[15] F. Boscaro, M. Palacios, R.J. Flatt, Formulation of low clinker blended cements and concrete with enhanced fresh and hardened properties, Cem. Concr. Res. 150 (2021) 106605, https://doi.org/10.1016/J.CEMCONRES.2021.106605.

[16] J.J. Thomas, H.M. Jennings, J.J. Chen, Influence of nucleation seeding on the hydration mechanisms of tricalcium silicate and cement, J. Phys. Chem. C 113 (2009) 4327–4334, https://doi.org/10.1021/jp809811w.

[17] R. Alizadeh, L. Raki, J.M. Makar, J.J. Beaudoin, I. Moudrakovski, Hydration of tricalcium silicate in the presence of synthetic calcium-silicate-hydrate, J. Mater. Chem. 19 (2009) 7937–7946, https://doi.org/10.1039/b910216g.

[18] P. Bost, M. Regnier, M. Horgnies, Comparison of the accelerating effect of various additions on the early hydration of Portland cement, Construct. Build Mater. 113 (2016) 290–296, https://doi.org/10.1016/j.conbuildmat.2016.03.052.

[19] A. Morales-Cantero, A. Cuesta, A.G. De la Torre, I. Santacruz, O. Mazanec, P. Borralleras, K.S. Weldert, D. Gastaldi, F. Canonico, M.A.G. Aranda, C-S-H seeding activation of Portland and Belite cements: an enlightening in situ synchrotron powder diffraction study, Cem. Concr. Res. 161 (2022) 106946, https://doi.org/10.1016/j.cemconres.2022.106946.

[20] A. Morales-Cantero, A. Cuesta, A.G. De la Torre, O. Mazanec, P. Borralleras, K. S. Weldert, D. Gastaldi, F. Canonico, M.A.G. Aranda, Portland and Belite cement hydration acceleration by C-S-H seeds with variable w/c ratios, Materials (Basel) 15 (2022) 3553, https://doi.org/10.3390/MA15103553.

[21] H. Li, Y. Xiang, C. Xu, Effect of C–S–H seed/PCE nanocomposites and triisopropanolamine on portland cement properties: hydration kinetic and strength, J. Build. Eng. 57 (2022) 104946, https://doi.org/10.1016/j.jobe.2022.104946.

[22] C. Redondo-Soto, A. Morales-Cantero, A. Cuesta, I. Santacruz, D. Gastaldi, F. Canonico, M.A.G. Aranda, Limestone calcined clay binders based on a Belite-rich cement, Cem. Concr. Res. 163 (2023) 107018, https://doi.org/10.1016/j.cemconres.2022.107018.

[23] G. Liang, D. Ni, H. Li, B. Dong, Z. Yang, Synergistic effect of EVA, TEA and C-S-Hs-PCE on the hydration process and mechanical properties of Portland cement paste at early age, Construct. Build Mater. 272 (2021) 121891, https://doi.org/10.1016/j.conbuildmat.2020.121891.

[24] J. He, G. Long, K. Ma, Y. Xie, Z. Cheng, Improvement of the hydration of a fly ash-cement system by the synergic action of triethanolamine and C-S-H seeding, ACS Sustain. Chem. Eng. 9 (2021) 2804–2815, https://doi.org/10.1021/acssuschemeng.0c08618.

[25] X. Chen, X. Yang, K. Wu, Q. Chen, Z. Yang, L. Xu, H. Li, Understanding the role of C – S – H seed / PCE nanocomposites , triethanolamine, sodium nitrate and PCE on hydration and performance at early age, Cem. Concr. Compos. 139 (2023) 105002, https://doi.org/10.1016/j.cemconcomp.2023.105002.

[26] A. Cuesta, A. Morales, A.G. De la Torre, M.A.G. Aranda, Recent advances in C-S-H nucleation seeding for improving cement performances, Materials (Basel) 16 (2023) 1462, https://doi.org/10.3390/ma16041462.
[27] E. John, T. Matschei, D. Stephan, Nucleation seeding with calcium silicate hydrate – a review, Cem. Concr. Res. 113 (2018) 74–85, https://doi.org/10.1016/j.cemconres.2018.07.003.
[28] G. Artioli, G. Ferrari, M.C. Dalconi, L. Valentini, Nanoseeds as modifiers of the cement hydration kinetics, in: M. Shahir Liew, P. Nguyen-Tri, T.A. Nguyen, S. Kakooei (Eds.), Smart Nanoconcretes Cem. Mater. Prop. Model. Appl, Elsevier, 2020, pp. 257–269, https://doi.org/10.1016/B978-0-12-817854-6.00010-6.
[29] X. Li, J. Bizzozero, C. Hesse, Impact of C-S-H seeding on hydration and strength of slag blended cement, Cem. Concr. Res. 161 (2022) 106935, https://doi.org/10.1016/j.cemconres.2022.106935.
[30] V. Kanchanason, J. Plank, Effect of calcium silicate hydrate – polycarboxylate ether (C-S-H–PCE) nanocomposite as accelerating admixture on early strength enhancement of slag and calcined clay blended cements, Cem. Concr. Res. 119 (2019) 44–50, https://doi.org/10.1016/J.CEMCONRES.2019.01.007.
[31] C. Ouellet-Plamondon, S. Scherb, M. Köberl, K.C. Thienel, Acceleration of cement blended with calcined clays, Construct. Build Mater. 245 (2020) 118439, https://doi.org/10.1016/J.CONBUILDMAT.2020.118439.
[32] D. Zhao, R. Khoshnazar, Hydration and microstructural development of calcined clay cement paste in the presence of calcium-silicate-hydrate (C–S–H) seed, Cem. Concr. Compos. 122 (2021) 104162, https://doi.org/10.1016/j.cemconcomp.2021.104162.
[33] X. Li, J. Dengler, C. Hesse, Reducing clinker factor in limestone calcined clay-slag cement using C-S-H seeding – a way towards sustainable binder, Cem. Concr. Res. 168 (2023) 107151, https://doi.org/10.1016/J.CEMCONRES.2023.107151.
[34] M. Zhang, L. Yang, F. Wang, Influence of C–S–H seed and sodium sulfate on the hydration and strength of limestone calcined clay cement, J. Clean. Prod. 408 (2023) 137022, https://doi.org/10.1016/J.JCLEPRO.2023.137022.
[35] A. Morales-Cantero, A.G. De la Torre, A. Cuesta, I. Santacruz, O. Mazanec, A. Dalla-Libera, S. Dhers, P. Borralleras, M.A.G. Aranda, Activation of LC3 low-carbon cements by C-S-H seeding, in: Proc. 16th Int. Congr. Chem. Cem. - Vol I, Bangkok, 2023, pp. 247–250, https://doi.org/10.13140/RG.2.2.26594.09920.
[36] A. Cuesta, A. Morales-Cantero, A.G. De la Torre, I. Santacruz, O. Mazanec, A. Dalla-Libera, S. Dhers, P. Schwesig, P. Borralleras, M.A.G. Aranda, Activation of LC3 binders by C-S-H nucleation seeding with a new tailored admixture for low-carbon cements, Ce/Papers - Proc. Civ. Eng. 6 (2023) 446–453, https://doi.org/10.1002/cepa.2786.
[37] J. Beaudoin, I. Odler, Hydration, setting and hardening of Portland cement, Lea's Chem. Cem. Concr. (2019) 157–250, https://doi.org/10.1016/B978-0-08-100773-0.00005-8.
[38] A. Cuesta, J.D. Zea-Garcia, D. Londono-Zuluaga, A.G. De la Torre, I. Santacruz, O. Vallcorba, M. Dapiaggi, S.G. Sanfélix, M.A.G. Aranda, Multiscale understanding of tricalcium silicate hydration reactions, Sci. Rep. 8 (2018) 8544, https://doi.org/10.1038/s41598-018-26943-y.
[39] B.Z. Dilnesa, E. Wieland, B. Lothenbach, R. Dähn, K.L. Scrivener, Fe-containing phases in hydrated cements, Cem. Concr. Res. 58 (2014) 45–55, https://doi.org/10.1016/j.cemconres.2013.12.012.
[40] M. Vespa, E. Wieland, R. Dähn, B. Lothenbach, Identification of the thermodynamically stable Fe-containing phase in aged cement pastes, J. Am. Ceram. Soc. 98 (2015) 2286–2294, https://doi.org/10.1111/jace.13542.
[41] F. Avet, X. Li, K.L. Scrivener, Determination of the amount of reacted metakaolin in calcined clay blends, Cem. Concr. Res. 106 (2018) 40–48, https://doi.org/10.1016/J.CEMCONRES.2018.01.009.
[42] F. Zunino, Y. Dhandapani, M. Ben Haha, J. Skibsted, S. Joseph, S. Krishnan, A. Parashar, M.C.G. Juenger, T. Hanein, S.A. Bernal, K.L. Scrivener, F. Avet, Hydration and mixture design of calcined clay blended cements: review by the RILEM TC 282-CCL, Mater. Struct. Constr. 55 (2022) 234, https://doi.org/10.1617/s11527-022-02060-1.
[43] S. Shirani, A. Cuesta, A. Morales-Cantero, A.G. De la Torre, M.P. Olbinado, M.A. G. Aranda, Influence of curing temperature on belite cement hydration: a comparative study with Portland cement, Cem. Concr. Res. 147 (2021) 106499, https://doi.org/10.1016/j.cemconres.2021.106499.
[44] C.E. White, J.L. Provis, T. Proffen, D.P. Riley, J.S.J. Van Deventer, Density functional modeling of the local structure of kaolinite subjected to thermal dehydroxylation, J. Phys. Chem. A 114 (2010) 4988–4996, https://doi.org/10.1021/jp911108d.
[45] C.E. White, J.L. Provis, T. Proffen, D.P. Riley, J.S.J. Van Deventer, Combining density functional theory (DFT) and pair distribution function (PDF) analysis to solve the structure of metastable materials: the case of metakaolin, Phys. Chem. Chem. Phys. 12 (2010) 3239–3245, https://doi.org/10.1039/b922993k.
[46] M.G. Muraleedharan, H. Asgar, S. Mohammed, G. Gadikota, A.C.T. Van Duin, Elucidating thermally induced structural and chemical transformations in kaolinite using reactive molecular dynamics simulations and X-ray scattering measurements, Chem. Mater. 32 (2020) 651–662, https://doi.org/10.1021/acs.chemmater.9b03929.
[47] J. Skibsted, R. Snellings, Reactivity of supplementary cementitious materials (SCMs) in cement blends, Cem. Concr. Res. 124 (2019) 105799, https://doi.org/10.1016/J.CEMCONRES.2019.105799.
[48] K. Weise, N. Ukrainczyk, E. Koenders, Pozzolanic reactions of metakaolin with calcium hydroxide: review on hydrate phase formations and effect of alkali hydroxides, carbonates and sulfates, Mater. Des. 231 (2023) 112062, https://doi.org/10.1016/J.MATDES.2023.112062.
[49] A.G. De la Torre, S. Bruque, M.A.G. Aranda, Rietveld quantitative amorphous content analysis, J. Appl. Cryst. 34 (2001) 196–202, https://doi.org/10.1107/S0021889801002485.
[50] F. Fauth, I. Peral, C. Popescu, M. Knapp, The New Material Science Powder Diffraction Beamline at ALBA Synchrotron, Cambridge University Press, 2013, https://doi.org/10.1017/S0885715613000900.
[51] B.H. Toby, R.B. Von Dreele, IUCr, GSAS-II: the genesis of a modern open-source all purpose crystallography software package, Urn:Issn:0021–8898 46 (2013) 544–549, https://doi.org/10.1107/S0021889813003531.
[52] I.R. Salcedo, A. Cuesta, S. Shirani, L. León-Reina, M.A.G. Aranda, Accuracy in cement hydration investigations: combined X-ray microtomography and powder diffraction analyses, Materials (Basel) 14 (2021) 6953, https://doi.org/10.3390/MA14226953.
[53] A.C. Larson, R.B. Von Dreele, General structure analysis system (GSAS), Los Alamos Natl. Lab. Rep. LAUR. 748 (2004) 86–748.
[54] L. Nicoleau, E. Jetzlsperger, D. Fridrich, M. Vierle, K. Lorenz, G. Albrecht, D. Schmitt, T. Wohlhaupter, R. Dorfner, H. Leitner, M. Bräu, C. Hesse, P. S. Montero, S. Zürn, M. Kutschera, Plasticizer-containing hardening accelerator composition, WO2010026155A1, WO2010026155A1. https://patents.google.com/patent/WO2010026155A1/en, 2010.
[55] A. Alzaza, K. Ohenoja, I. Langås, B. Arntsen, M. Poikelispää, M. Illikainen, Low-temperature (−10 °C) curing of Portland cement paste – Synergetic effects of chloride-free antifreeze admixture, C–S–H seeds, and room-temperature pre-curing, Cem. Concr. Compos. 125 (2022) 104319, https://doi.org/10.1016/j.cemconcomp.2021.104319.
[56] H.C. Pedrosa, O.M. Reales, V.D. Reis, M. das D. Paiva, E.M.R. Fairbairn, Hydration of Portland cement accelerated by C-S-H seeds at different temperatures, Cem. Concr. Res. 129 (2020) 105978, https://doi.org/10.1016/j.cemconres.2020.105978.
[57] L. Nicoleau, The acceleration of cement hydration by seeding: influence of the cement mineralogy, ZKG Int. 40–49 (2013).
[58] L. Huang, Z. Yang, Hydration kinetics of tricalcium silicate with the presence of portlandite and calcium silicate hydrate, Thermochim. Acta 681 (2019) 178398, https://doi.org/10.1016/j.tca.2019.178398.
[59] J. Lee, B. Lothenbach, J. Moon, Performance improvement of Portland-limestone cement by mechanochemical activation, Cem. Concr. Res. 176 (2024) 107411, https://doi.org/10.1016/J.CEMCONRES.2023.107411.
[60] L. Nicoleau, E. Schreiner, A. Nonat, Ion-specific effects influencing the dissolution of tricalcium silicate, Cem. Concr. Res. 59 (2014) 118–138, https://doi.org/10.1016/j.cemconres.2014.02.006.
[61] E. Pustovgar, R.K. Mishra, M. Palacios, J.-B. d'Espinose de Lacaillerie, T. Matschei, A.S. Andreev, H. Heinz, R. Verel, R.J. Flatt, Influence of aluminates on the hydration kinetics of tricalcium silicate, Cem. Concr. Res. 100 (2017) 245–262, https://doi.org/10.1016/j.cemconres.2017.06.006.
[62] D. Wagner, F. Bellmann, J. Neubauer, Influence of aluminium on the hydration of triclinic C3S with addition of KOH solution, Cem. Concr. Res. 137 (2020) 106198, https://doi.org/10.1016/j.cemconres.2020.106198.
[63] T. Hirsch, Z. Lu, D. Stephan, Effect of different sulphate carriers on Portland cement hydration in the presence of triethanolamine, Construct. Build Mater. 294 (2021) 123528, https://doi.org/10.1016/j.conbuildmat.2021.123528.
[64] F. Zunino, K.L. Scrivener, The influence of the filler effect on the sulfate requirement of blended cements, Cem. Concr. Res. 126 (2019) 105918, https://doi.org/10.1016/j.cemconres.2019.105918.
[65] G. Artioli, L. Valentini, M.C. Dalconi, M. Parisatto, M. Voltolini, V. Russo, G. Ferrari, Imaging of nano-seeded nucleation in cement pastes by X-ray diffraction tomography, Int. J. Mater. Res. 105 (2014) 628–631, https://doi.org/10.3139/146.111049.
[66] F. Avet, K.L. Scrivener, Investigation of the calcined kaolinite content on the hydration of limestone calcined clay cement (LC3), Cem. Concr. Res. 107 (2018) 124–135, https://doi.org/10.1016/j.cemconres.2018.02.016.
[67] F. Zunino, K.L. Scrivener, Assessing the effect of alkanolamine grinding aids in limestone calcined clay cements hydration, Construct. Build Mater. 266 (2021) 121293, https://doi.org/10.1016/j.conbuildmat.2020.121293.
[68] H. Huang, X. Li, F. Avet, W. Hanpongpun, K. Scrivener, Strength-promoting mechanism of alkanolamines on limestone-calcined clay cement and the role of sulfate, Cem. Concr. Res. 147 (2021) 106527, https://doi.org/10.1016/j.cemconres.2021.106527.
[69] Y. Briki, F. Avet, M. Zajac, P. Bowen, M. Ben Haha, K. Scrivener, Understanding of the factors slowing down metakaolin reaction in limestone calcined clay cement (LC3) at late ages, Cem. Concr. Res. 146 (2021) 106477, https://doi.org/10.1016/j.cemconres.2021.106477.
[70] Z. Casar, A.K. Mohamed, P. Bowen, K. Scrivener, Atomic-level and surface structure of calcium silicate hydrate nanofoils, J. Phys. Chem. C 127 (2023) 18652–18661, https://doi.org/10.1021/ACS.JPCC.3C03350.
[71] A. Cuesta, I. Santacruz, A.G. De la Torre, M. Dapiaggi, J.D. Zea-Garcia, M.A. G. Aranda, Local structure and Ca/Si ratio in C-S-H gels from hydration of blends of tricalcium silicate and silica fume, Cem. Concr. Res. 143 (2021) 106405, https://doi.org/10.1016/j.cemconres.2021.106405.
[72] X. Zhu, I.G. Richardson, Morphology-structural change of C-A-S-H gel in blended cements, Cem. Concr. Res. 168 (2023) 107156, https://doi.org/10.1016/j.cemconres.2023.107156.